• U C •

FCTUC FACULDADE DE CIÊNCIAS
E TECNOLOGIA
UNIVERSIDADE DE COIMBRA

DEPARTAMENTO DE
ENGENHARIA MECÂNICA

Dynamic response of WC-Ni powder

Submitted in Partial Fulfilment of the Requirements for the Master Degree in Mechanical Engineering in the speciality of Production and Project

Comportamento dinâmico do pó WC-Ni

Author

Mário Rui Adrião Gonçalves

Advisors

José Manuel Baranda Moreira da Silva Ribeiro

Cristina Maria Gonçalves dos Santos

Jury

President	**Professor Doutor Fernando Jorge Ventura Antunes** **Professor da Universidade de Coimbra**
Vowels	**Professor Doutor José Maria Osório de Sousa Cirne** **Professor da Universidade de Coimbra**
	Professor Doutor Ricardo António Lopes Mendes **Professor da Universidade de Coimbra**
	Professor Doutor Cristina Maria Gonçalves dos Santos **Professor da Universidade de Coimbra**

Institutional Collaboration

Institute of Shock Physics

Institute of Shock Physics, Imperial College London

Coimbra, September, 2016

“Eu vo-lo digo: é preciso ter um caos dentro de si para dar à luz uma estrela cintilante”

Friedrich Nieztsche.

ACKNOWLEDGEMENTS

The work presented here was only possible due to the collaboration and support of some people, which I have to show my gratitude.

I would like to thank Doctor W. G. Proud, Professor José Baranda and Professor Cristina Santos for the invitation to do my master thesis at Institute of Shock Physics, Imperial College London. I also want to thank the availability they always have demonstrated to help me.

I would like to thank Doctor J.P. Duarte for helping me on the multiple target setup design for planar shock impact study.

I would like to thank Mr. Paul Brown and the rest of the Mechanical Instrumentation Workshop, from Imperial College, for their work on the components manufacturing all the parts necessary for the experimental work.

I need to show also, all my gratitude to Mr. David Sory, PhD student from Institute of Shock Physics at Imperial College, that since the beginning helped me not only with SHPB experiments but also led me to make the best decisions for project.

Finally, I would like to thank my family and friends for all the support and energy that they gave me during these 6 months in England.

Abstract

Dynamic behavior of WC-Ni system powder, containing 9 wt.% Ni, was investigated.

From medium strain rates, the Spilt Hopkinson Pressure Bar (SHPB) method was selected. The design of the Hopkinson bar experiment was modified in order to study the stress and strain states as well as the sound speed in the powder during the dynamic loading. The powder specimen was confined in a sleeve and was loaded by mean of Hopkinson bars in order to get the axial stress and the strain in the sample. Hoop strain gauge was glued in a confining sleeve allowing the deduction of the radial stress in the specimen.

To investigate the WC-9Ni powder behavior at high strain rates a multiple target setup was designed. In this case, the Hugoniot properties were measured under a planar shock wave by using a gas-gun. The multiple target was specially designed to hold 3 specimens.

From the SHPB compression tests a particular behavior was observed during the dynamic compaction, wherein two phases were identified but the effects were not well recognized.

Keywords Shock wave, dynamic loading, strain gauges, Hugoniot properties, sound speed, strain rate.

Resumo

Este trabalho teve principal objetivo estudar o comportamento dinâmico do sistema WC-Ni, Ni = 9%pd, sob a forma de pó.

Para taxas médias de deformação utilizou-se a técnica experimental Split Hopkinson Pressure Bar (SHPB). Os resultados obtidos, no que concerne os estados de tensão e de deformação, assim como a velocidade do som no pó durante a ação de uma carga dinâmica, foram conseguidos por modificação da conceção da SHPB. Após colocação da amostra em pó num tubo, este foi comprimido por ação das barras de Hopkinson. Conseguiu obter-se a tensão e a deformação axial na amostra WC-9Ni. Foi ainda necessário colocar um extensómetro na direção circunferencial do tubo contendo o material de forma a estimar-se o valor de tensão radial na amostra.

Para taxas elevadas de deformação, as propriedades de Hugoniot do material em pó foram avaliadas por onda de choque plana utilizando um canhão de gás. Para tal projetou-se uma configuração de alvos múltiplos de modo a conter três grupos de amostras.

A partir dos ensaios de compressão SHPB observou-se um comportamento dinâmico particular do sistema WC-9Ni, tendo sido identificadas duas fases. As causas para tal comportamento permanecem por esclarecer.

.

Palavras-chave: Onda de choque, carga dinâmica, extensómetros, propriedades de Hugoniot, velocidade do som, taxa de deformação.

Contents

LIST OF FIGURES

LIST OF TABLES

SIMBOLOGY AND ACRONYMS

Simbology

$\dot{u_A}(t)$ – Particle velocity of incident bar

$\dot{u_B}(t)$ – Particle velocity of transmitter bar

$\dot{\varepsilon_s}(t)$ – Strain rate in the specimen

$\varepsilon_\theta{}^{ext}$ – External hoop strain in the sleeve

$\overline{\sigma_s}(t)$ – Average axial stress in the specimen

Δt_s, Δt_{blank} – Interval of time between the first signal of the transmitted and incident wave, for a test with specimen and without specimen

Δt_t – Time that the wave takes to travel along the specimen`s thickness

A_b – Bars cross-sectional area

$A_s(t)$ – Instantaneous specimen cross-sectional area

C_b – Bars sound speed

C_s – Sound speed in the specimen

E_b – Bars Young`s Modulus

E_s – Young`s Modulus of the specimen

$F_A(t)$ – Force in the incident bar-specimen interface

$F_B(t)$ – Force in the transmitter bar-specimen interface

$F_{inc}(t)$ – Force in incident bar

$F_{tran}(t)$ – Force in transmitter bar

L_s – Initial specimen`s thickness

L_{sb} – Striker bar length

L_{strip} – Strips length

P_0, P_1 – Pressure in unshocked and shocked region

P_{hydr} – Hydrostatic pressure

P_i – Internal pressure in of the sleeve

R_e – External radius of the sleeve

R_i – Internal radius of the sleeve

U_s – Shock wave velocity

$\overline{V}$ – Average voltage of longitudinal pulse

V_{impact} – Flier impact velocity

$V^{scaled}(t)$ – Scaling signal for attenuation waves in the bars

V_θ – Hoop gauge voltage signal

Z_b, Z_{sb} – Impedance of bars

c_0, c_1, c_2 – Fitting coefficients of attenuation waves in the bars

c_L – Longitudinal wave velocity

e_0, e_1 – Energy per unit mass in unshocked and shocked region

k_1, k_2 – Coefficients of incident and transmitter bars calibration

m_{sb} – Striker bar mass

t_l – Duration of longitudinal pulse

u_0, u_p – Particle velocity in unshocked and shocked region

u_A – Displacement of the incident bar

u_B – Displacement of the transmitter bar

v_0, v_1 – Specific volume in unshocked and shocked region

$\varepsilon_A(t)$ – Longitudinal elastic strain of incident bar

$\varepsilon_B(t)$ – Longitudinal elastic strain of transmitter bar

$\varepsilon_i(t)$ – Longitudinal incident wave

ε_n – Axial strain in the specimen for elastic-plastic model

$\varepsilon_r(t)$ – Longitudinal reflected wave

$\varepsilon_s(t)$ – Longitudinal strain in the specimen

$\varepsilon_t(t)$ – Longitudinal transmitted wave

ρ_0, ρ_1 – Density in unshocked and shocked region

ρ_b – Bars density

ρ_s – Specimen`s density

ρ_{powder} – Theoretical density of the powder

σ^E – Stress in elastic regime

σ_H – Hugoniot Elastic Limit of stress

σ_{Tr} – Equivalent stress in the sleeve according to Tresca yield theory

σ_Y – Yield stress in the sleeve

σ_n – Stress of elastic-plastic model

σ_r – Radial stress in the inner surface of the sleeve

$\sigma_s(t)$ – Axial stress in the specimen

σ_θ – Hoop stress in the inner surface of the sleeve

σ_θ – Hoop stress in the sleeve

ΔR – Electric resistance change

ΔV – Electric potential difference

A – Cross-sectional area of shocked region

K – Stress concentration factor for tubes

L – Final specimen`s thickness

$V(t)$ – Voltage of longitudinal pulse

Y – Yield stress

a, b – constant coefficients of the shocked material

f, g, h – Arbitrary functions

m – mass of the specimen

p – hydrodynamic pressure

$\gamma(t)$ – Scaling factor for attenuation waves in the bars

σ – Stress

∂u – Displacement of a differential element

∂x – Length of a differential element

Acronyms

ID – Inner diameter

OD – Outer diameter

PMMA – Polymethyl methacrylate

RD – Relative density

SEM – Scanning Electron Microscope

SHPB – Split Hopkinson Pressure Bar

W – Tungsten

WC – Tungsten carbide

1. INTRODUCTION

The tungsten carbide is one of the materials widely used to produce cutting tools, molds, machines and tools for extractive industry due to its excellent mechanical properties as: high hardness, high wear resistance, high melting temperature and high thermal and electrical conductivity. In the last years, the binder cobalt has been replaced by the nickel due to the good corrosion resistance of the nickel and for this reason the tungsten carbide with nickel as a binder is studied in this project. The production of parts by processing powders is a very attractive technology wherein using only one operation it is possible to produce parts near from the final shape. Some problems have arisen during the sintering process because of the long time and high temperatures that the parts are exposed, changing the properties of the materials during this operation. As a solution for this problems, the dynamic compaction has been studied with the aim of increase the initial density before the sintering process, reducing the time and temperature of this process.

In dynamic compaction technology, explosives are used to create a shock wave, which will compact the material and for this reason it is very important to characterize the behaviour of this material under dynamic loading which is the focus of this project. SHPB apparatus and gas-gun can be used to study the behavior of the (WC-9wt%Ni) powder for a widely range of strain rates. The dynamic properties at medium strain rates will be studied using a modified SHPB apparatus. No literature about tungsten carbide powder using this technique was found, however, this has been used to study the dynamic response of others granular materials. Proud et al. (2007) investigated sand, Forquin et al. (2008) studied concrete and Häggblad et al. (2005) characterized titanium powder. In all cases the specimen is confined in a sleeve, wherein the specimen is compressed using SHPB bars.

Unfortunately, the dynamic properties at high strain rates and pressures greater than 1 GPa was not studied due to logistic issues, which did not allow to do the gas-gun experimental tests at time. However, a target setup was designed to conduct a planar shock wave in the specimens. The behavior of tungsten carbide powder under shock waves has been studied over several years in order to understand the mechanisms of deformation and its non-linear response. McQueen (1970) studied the Hugoniot shock near full density

tungsten carbide with 5wt% Co and Grady (1995, 1999) reported shock data of two types of WC materials.

In this work a particular focus will be given for the SHPB apparatus, wherein methods are developed in order to analyse the stress-stain states and sound speed in the powder. In chapter 2 a theoretical background is presented about SHPB theory and planar shock waves theory in condensed material. The chapter 3 begins with a brief characterization of WC-Ni powder and then is presented the SHPB apparatus, wherein the method to determine the stress- strain states and sound speed is introduced. Lastly, in this chapter is presented the multiple target for gas-gun experiments, as well as a brief description of the data analysis. In chapter 4, the results of the SHPB experiment are shown, as well as a discussion of the results. The chapter 5 reports the main conclusion of the project, wherein some recommendations are provided.

2. BACKGROUND

2.1. Split Hopkinson Bar system

The Split Hopkinson Bar was design to characterize a variety of material types under compression, tension and shear at medium strain rates. The SHPB system is used to create a dynamic compressive loading which allows to describe the stress and strain states in the specimen. The Figure 2.1 shows a common SHPB apparatus to study a material under compression. This apparatus is composed by a pressure air chamber, a striker bar, sensing devices to measure the striker bar velocity, two long bars that can be symmetric, a specimen between the bars, a support system that allows the bars to move freely, strain gauges assembled on both bars and a recording system which is composed by two Wheatstone Bridges and a digital oscilloscope.

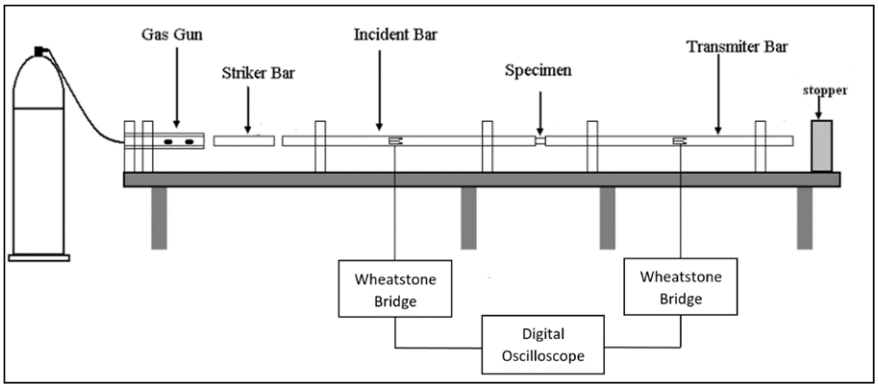

Figure 2.1. A common compression SHPB apparatus (S. Sharma et al., 2011).

Compressed air in a chamber is release to launch the striker bar which impacts at the free surface end of the incident bar that generates a longitudinal compressive wave, $\varepsilon_i(t)$, in the incident bar. When the incident wave has reached the interface between specimen and incident bar, part of it is reflected into the incident bar, $\varepsilon_r(t)$, and part is transmitted to the specimen. Once the compressive wave reaches the interface between specimen and transmitter bar, part of it is transmitted to the transmitter bar, $\varepsilon_t(t)$, and part is reflected into the specimen as illustrated in Figure 2.2. It is important to notice in this

figure, that the striker bar hits the incident bar from the right to the left, while in Figure 2.1 the striker bar comes from the opposite direction.

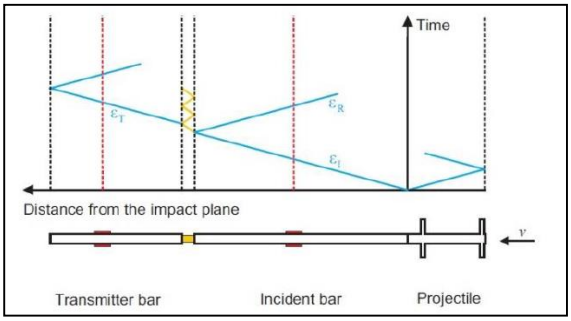

Figure 2.2. Stress pulse propagation along the setup (Sory, 2013).

The incident and the reflected waves are picked up by the strain gauge in the incident bar and the transmitted wave is picked up by the strain gauge in the transmitter bar as show in Figure 2.3, wherein this case the strain gauges are not positioned equidistant from the specimen in the axial direction. The strain gauges are located in incident and transmitter bars, such that incident and reflected wave do not overlap during the measurement of the temporal evolution of the waves. The Wheatstone Bridge is connected between each strain gauge and the oscilloscope which allows the measurement of the electric resistance change (ΔR) in the gauges and relate it regarding the electric potential difference (ΔV) that is recorded by the oscilloscope.

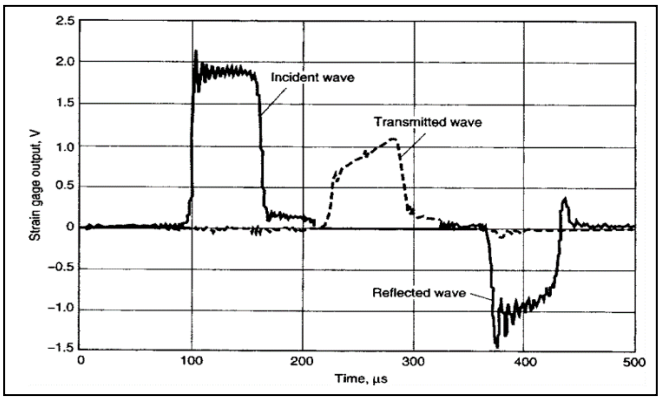

Figure 2.3. Strain gauge`s signals obtained for 304L stainless steel (Gama et al., 2004).

2.1.1. Compression SHPB theory

Since the bars remain in elastic regime and the ratio length/diameter of the incident and transmitter bars is great enough, one dimensional elastic wave model can be assumed, as reported, for example, by Lang (2012). From this, the stress and deformation at the bars end in contact with the specimen can be obtained, therefore, stress and strain states in the specimen can be calculated.

In one dimension (*x*), the relation stress-strain of the bars is:

$$\sigma = E_b \frac{\partial u}{\partial x} \tag{2.1}$$

where the E_b is the bars Young`s Modulus, u is the displacement of a differential element of a length ∂x in any position of the bars. The motion equation is:

$$\frac{\partial \sigma}{\partial x} = \rho_b \frac{\partial^2 u}{\partial t^2} \tag{2.2}$$

where ρ_b is the bars mass density. Relating equation (2.1) and (2.2), the equation (2.3) is obtained:

$$E_b \frac{\partial^2 u}{\partial x^2} = \rho_b \frac{\partial^2 u}{\partial t^2}. \tag{2.3}$$

It is known that the sound speed C_b which propagates in one dimension for free vibration is:

$$C_b = \sqrt{\frac{E_b}{\rho_b}}. \tag{2.4}$$

Combining equation (2.3) and (2.4), the motion equation in the bars can be described as:

$$C_b{}^2 \frac{\partial^2 u}{\partial x^2} = \frac{\partial^2 u}{\partial t^2}. \tag{2.5}$$

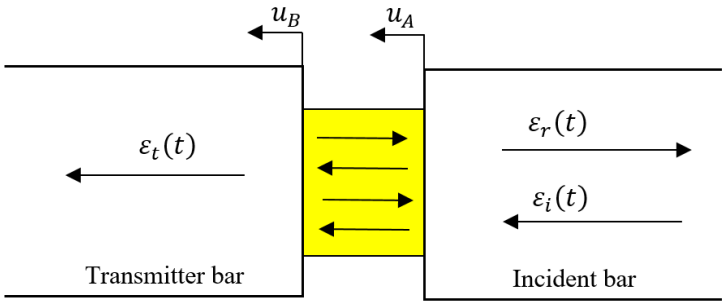

Figure 2.4. Expanded view of specimen placed between incident and transmitter bars.

Using the D`Alambert`s solution for the motion equation, the longitudinal displacement of the incident bar (u_A) and transmitter bar (u_B), which is the same as in the incident bar-specimen and transmitter bar-specimen interface, respectively, as shown in Figure 2.4, can assume the forms:

$$u_A = f(x - C_b t) + g(x + C_b t) \tag{2.6}$$

$$u_B = h(x - C_b t) \tag{2.7}$$

where f, g and h are arbitrary functions. The function $f(x - C_b t)$ and $g(x + C_b t)$ correspond to the incident and reflected wave, respectively, and the function $h(x - C_b t)$ corresponds to the transmitted wave. The elastic strain in the bars can be derived by differentiating equations (2.6) and (2.7) with respect to position ($\partial u/\partial x$), respectively, which results in:

$$\varepsilon_A(t) = f`(x - C_b t) + g`(x + C_b t) = \varepsilon_i(t) + \varepsilon_r(t) \tag{2.8}$$

$$\varepsilon_B(t) = h`(x - C_b t) = \varepsilon_t(t) \tag{2.9}$$

By differentiation equations (2.6) and (2.7) with respect to time ($\partial u/\partial t$), the particle velocity in the bars can be derived, resulting in:

$$\dot{u_A}(t) = -C_b \times f`(x - C_b t) + C_b \times g`(x + C_b t) = -C_b[\varepsilon_i(t) - \varepsilon_r(t)] \quad (2.10)$$

$$\dot{u_B}(t) = -C_b h`(x - C_b t) = -C_b \varepsilon_t(t) \quad (2.11)$$

The strain rate in the specimen can be defined as,

$$\dot{\varepsilon_s}(t) = \frac{\dot{u_A}(t) - \dot{u_B}(t)}{L_s} = -\frac{C_b}{L_s}[\varepsilon_i(t) - \varepsilon_r(t) - \varepsilon_t(t)] \quad (2.12)$$

where L_s is the initial specimen`s thickness. By integrating the strain rate, the axial strain in the specimen can be calculated, which gives:

$$\varepsilon_s(t) = -\frac{C_b}{L_s}\int_{t_1}^{t_2}[\varepsilon_i(t) - \varepsilon_r(t) - \varepsilon_t(t)]\, dt \quad (2.13)$$

Applying the Hook`s law, the forces in the bars-specimen interface can be determined from incident and transmitter gauges, respectively, as:

$$F_A(t) = A_b E_b \varepsilon_A(t) = A_b E_b[\varepsilon_i(t) + \varepsilon_r(t)] \quad (2.14)$$

$$F_B(t) = A_b E_b \varepsilon_B(t) = A_b E_b[\varepsilon_t(t)] \quad (2.15)$$

where A_b is the bars cross-sectional area. The average stress in the specimen can be expressed as the forces average that acts in the bars-specimen interface, which gives:

$$\overline{\sigma_s}(t) = \frac{A_b E_b}{2 \times A_s(t)}[\varepsilon_i(t) + \varepsilon_r(t) + \varepsilon_t(t)] \quad (2.16)$$

where $A_s(t)$ is the instantaneous specimen cross-sectional area. If the specimen reaches the dynamic stress equilibrium, which means that the forces in the bars-specimen interfaces are the same ($F_A = F_B$), the stress in the specimen can be calculated using incident or transmitter gauges (two waves or one wave analysis), respectively, by the following equations:

$$\sigma_s(t) = \frac{A_b E_b}{A_s(t)}[\varepsilon_i(t) + \varepsilon_r(t)] \tag{2.17}$$

$$\sigma_s(t) = \frac{A_b E_b}{A_s(t)}[\varepsilon_t(t)] \tag{2.18}$$

2.2. Shock waves

In physics, a shock wave is a waves which propagates faster than the speed of sound in the medium and it is characterized by a sharply and almost discontinuous change in pressure, density and energy. In the shock wave field, for a better understanding of this phenomena there are some assumptions that are used, as described by Forbes (2012). The parameters that characterize a shock wave are the shock wave velocity, (U_s), particle velocity, (u_p), pressure, (P), energy per unit mass, (e), and density, ρ, or specific volume, v. It is important that during the measurement of these parameters a shock wave keeps steady in order to use the conservation laws to describe this phenomenon.

2.2.1. Hugoniot relations

A one-dimensional (1D) plane shock wave which propagates in a fluid (no strength) is assumed in order to use a basic physic and hydrodynamic analysis. Body forces are neglected and it is assumed that the material does not change phase. The laws of conservation of mass, momentum and energy can be applied to describe the initial and final states of the medium. In Figure 2.5 is illustrated a block of fluid where the shock wave propagates from the left (state 1) to the right (state 0). The interface between the shocked and unshocked fluid is the shock front which moves at the shock wave velocity, U_s. In the shocked region the particles move at the particle velocity, u_p, and in unshocked region the particles move at velocity, u_0.

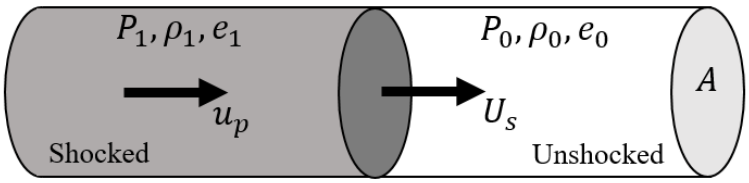

Figure 2.5. Propagation of a shock wave.

Applying the conservation of mass, the following equation can be determined:

$$\rho_0(U_s - u_0)A = \rho_1\big(U_s - u_p\big)A \tag{2.19}$$

where $\rho_0(U_s - u_0)A$ and $\rho_1\big(U_s - u_p\big)A$ is the mass per unit time ahead and behind the shock wave respectively. If the unshocked region is at rest, $u_0 = 0$, the jump of pressure can be related in terms of impulse which is conserved per unit time, resulting in the conservation of momentum given by the following equation:

$$\rho_1 u_p(U_s - u_p)A = (P_1 - P_0)A \tag{2.20}$$

where $\rho_1 u_p(U_s - u_p)A$ and $(P_1 - P_0)A$ are the impulse per unit time ahead and behind the shock wave respectively. Relating equations (2.19) and (2.20) the momentum equation is obtained:

$$P_1 - P_0 = \rho_0 U_s u_p \tag{2.21}$$

where is considered $P_0 \ll P_1$. The conservation of energy can also be applied where the work done by the pressure per unit time is equal to the change in kinetic and internal energy which is related by the following equation:

$$P_1 u_p A = \frac{1}{2}\rho_0 U_s {u_p}^2 A + \rho_0 U_s(e_1 - e_0)A. \tag{2.22}$$

Relating equations (2.21) and (2.22) the energy jump is given by,

$$e_1 - e_0 = \frac{1}{2}(P_1 + P_0)(v_0 - v_1). \tag{2.23}$$

For some materials the relation $U_s - u_p$ is presented as a linear equation,

$$U_s = a + bu_p \tag{2.24}$$

where a and b are constant coefficients of the material which are experimental determined. Thus, from the conservation equations and equation (2.24), the Principal Hugoniot paths, $(P - v)$ and $(P - u_p)$, can be determined by the following equations:

$$p = \frac{a^2(v_0 - v)}{(v_0 - b(v_0 - v))^2} \tag{2.25}$$

$$p = \rho_0(a + bu_p)u_p \tag{2.26}$$

where is considered $u_0 = 0$ and $P_0 = 0$. In Figure 2.6 is illustrated the Hugoniot paths, Forbes (2012), which are made up of end states that result from doing many experiments at different input stresses. It is also depicted the Rayleigh line which is a straight line with the equation $p = \rho_0 U_s u_p$, where $\rho_0 U_s$ is the shock impedance of the shocked material. This line is useful because it allows to get the end states of the material if the shock velocity, U_s, and initial density, ρ_0, are known.

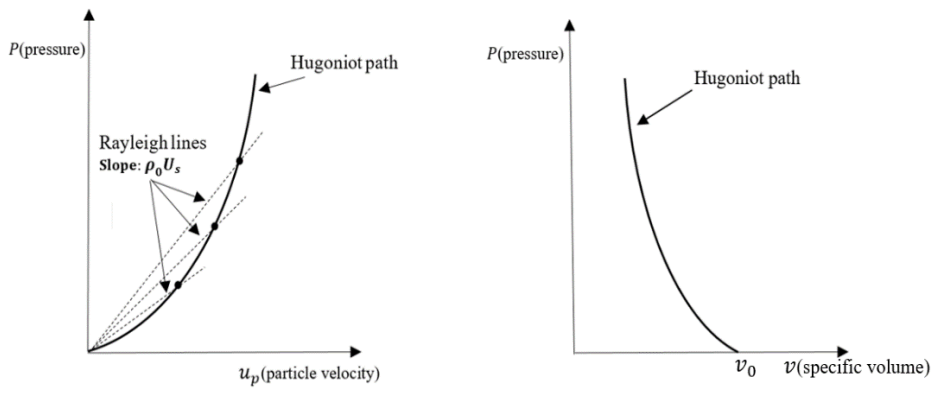

Figure 2.6. Hugoniot paths (Forbes, 2012).

2.2.2. Elastic-plastic model

As was referred in section 2.2.1, the material was assumed to act as a fluid, for solid material, which has elastic and plastic behavior, the model needs to be different. In plate impact test where there is 1D shock configuration, the material is in uniaxial strain because at high strain rates the material does not have time to flow in lateral direction. The stress-strain state evolution for uniaxial strain (Ron, 2009) can be seen in Figure 2.7. Thus, the axial strain in the specimen can be calculated by using equation (2.27).

$$\varepsilon_n = \ln\left(\frac{L_s}{L}\right) \tag{2.27}$$

where L_s and L are the initial and final specimen`s thickness.

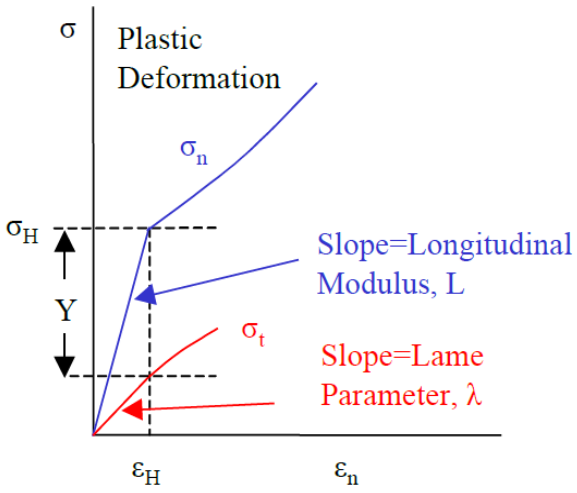

Figure 2.7. Stress-strain state for uniaxial strain (Ron, 2009).

A range of materials can be well described by the elastic-perfectly-plastic strength model, wherein the yield stress, Y, is a constant value in plastic regime and can be described by Tresca method, Winter (2009), as $Y = \sigma_n - \sigma_t$.

Hugoniot Elastic Limit, σ_H, is the value of axial stress, σ_n, at the point at which the material yield and σ_t is the transverse stress. In Figure 2.8 is shown the loading and unloading path for materials described by elastic-perfectly-plastic models where the loading path is 2/3 above the hydrostatic pressure while the unloading path is 2/3 below it.

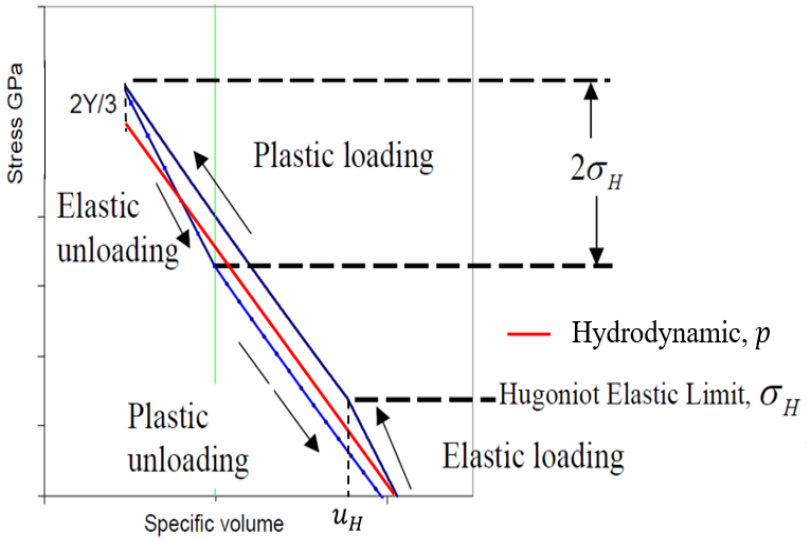

Figure 2.8. Loading and unloading path for elastic-perfectly-plastic model (Ron, 2009).

The stress in elastic regime can be described by the following equation:

$$\sigma^E = \rho_0 c_L u_p \tag{2.28}$$

where c_L is the longitudinal wave velocity.

For the plastic regime, the stress is related with hydrodynamic pressure (equation (2.26)) and the yield stress, which gives:

$$\sigma_n = p + \frac{2}{3}Y \tag{2.29}$$

3. MATERIALS AND METHODS

3.1. Materials

In this investigation the tungsten carbide with nickel as a binder was tested under dynamic loading. In the Table 3.1 the characteristics of the tungsten carbide grade are presented.

Table 3.1. Characteristics of WC-Ni powder

Powder	Ni (wt.%)	D_{50} (μm)	Density (g/cm^3)
WC-Ni	9	1.2	14.7

Microstructural characterization by Scanning Electron Microscope, SEM, of the particles are shown in Figure 3.1. It is possible to conclude that WC particles shape are rounded while the Ni particles presents an angular form.

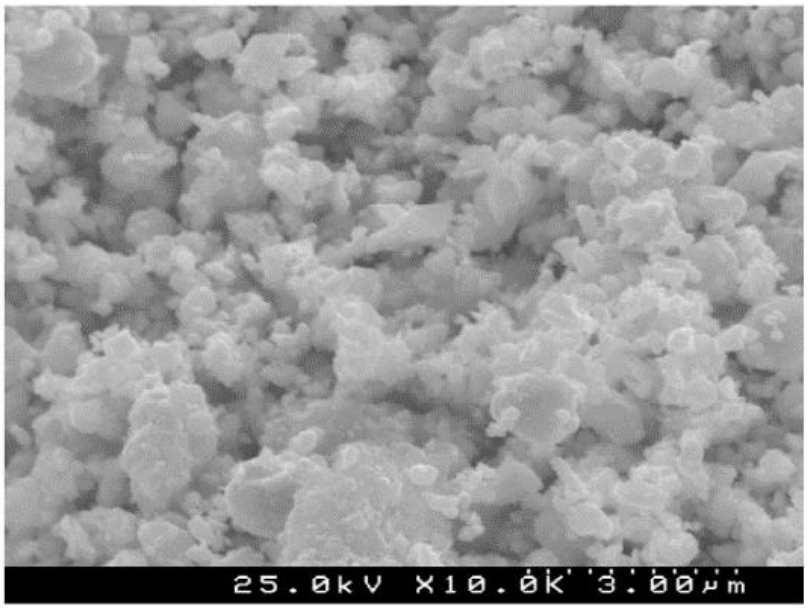

Figure 3.1. WC-Ni powder characterization by SEM (Pires, 2012).

3.2. Specimens` preparation

For the gas-gun experiment, a compressing dye device was designed in a hard steel to compress the powder in a certain relative density inside a ring, which is used to confine the specimen. This configuration, as illustrated in Figure 3.2, not only allows a uniform density of the specimen, but it also prevents the powder falling out inside of the confining ring and gets damaged while it is collected from the compressing dye. This device is composed by a punch to compress the powder, a body which is divided in two parts that are connected by two aligning pins and four screws. Between these two parts there is a hollow where the ring is placed, as well as a tube to align the punch. 2D drawings of compressing dye device can be consulted in ANNEX B.

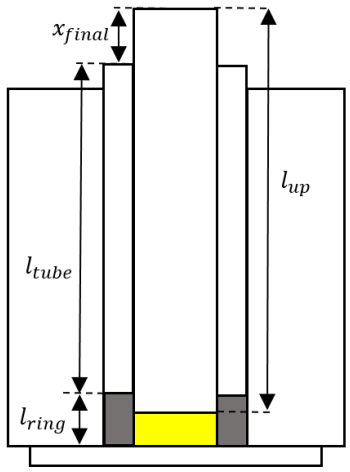

Figure 3.2. Preloading configuration for gas-gun experiment.

For the SHPB experiment, the configuration illustrated in Figure 3.3 was used to pre-compress the specimen, using a INSTRON machine. The role of the stepper rings and the bottom punch is to put the specimen in the desired position inside the confining sleeve in order that the hoop strain gauge will be in the middle of the specimen`s thickness. The powder was compressed between the bottom and the upper punches.

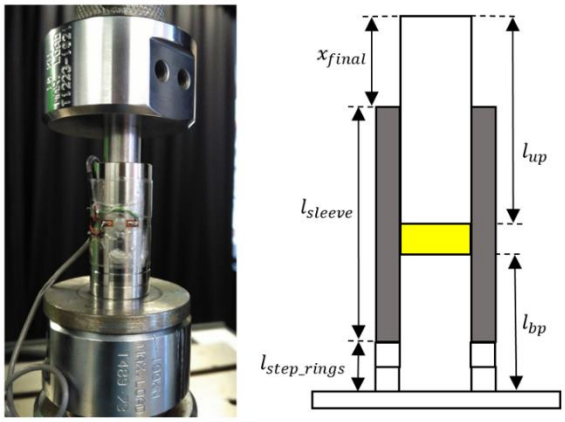

Figure 3.3. Preloading configuration for SHPB experiment using a INSTRON machine.

3.2.1. Confining sleeve and ring

A seamless stainless steel pipe (ASTM A790/A790M-10) with a nominal size (1/2`` SCH160) was purchased to manufacture the sleeve and ring, for SHPB and gas-gun experiments, respectively. The pipe was machined and cut with the desired dimensions presented in Table 3.2, where ID and OD represents, the inner and the outer diameters, respectively.

Table 3.2. Pipes dimensions

Pipe dimensions	ID (mm)	OD (mm)	Length (mm)
l_{sleeve} SHPB experiment	12.78	20.5	35
l_{ring} Gas gun experiment	12.1	20.5	4

3.2.2. Yield stress in the sleeve

In both pre-compaction and SHPB experiment the sleeves cannot deform plastically, thus, the yield stress of the sleeve cannot be attained. The producer provided a tensile test that is presented in Table 3.3.

Table 3.3. Tensile test

Pipe samples	T (ºC)	Rp0,2 (MPa)
1	20	711
2	20	696

The yield stress was, approximated, evaluated by the average of the Rp0.2. Thus the yield stress has a value of:

$$\sigma_Y \approx \frac{(Rp0{,}2_{test1} + Rp0{,}2_{test2})}{2} \approx \frac{(711 + 696)}{2} \approx 703\ MPa. \tag{3.1}$$

From the thick-walled cylinder theory, as reported by Ayob *et al.* (2009), the radial and hoop stress in the inner surface can be determined as:

$$\sigma_r = P_i \tag{3.2}$$

$$\sigma_\theta = P_i \left[\frac{{R_e}^2 + {R_i}^2}{{R_e}^2 - {R_i}^2}\right] \tag{3.3}$$

where P_i is the internal pressure in the sleeve and R_i and R_e are the internal e external radius of the sleeve, respectively. According to Tresca yield theory, (Ayob *et al.*, 2009), and knowing that the yielding start to occur in the inner surface, the equivalent stress is:

$$\sigma_{Tr} = \sigma_\theta - \sigma_r \leq \sigma_Y \tag{3.4}$$

It is important to highlight that the tests provided by the producer were made for the nominal size (1/2`` SCH160), which is thicker than the sleeve used. However, as it will be seen later, the yield stress is much superior than the equivalent stress in the sleeve during the SHPB tests.

3.2.3. Density measurement

The relative density (RD) of the pre-compacted specimens was determined by the following equation:

$$RD(\%) = \frac{\rho_s}{\rho_{powder}} = \frac{\dfrac{m}{L_s \times \pi \times \dfrac{ID^2}{4}}}{\rho_{powder}} \times 100 \tag{3.5}$$

where the ρ_{powder} is the theoretical density of the powder, ρ_s is the relation of mass (m) placed inside the sleeve divided by the volume of the specimen, which has a diameter (ID) and a thickness (L_s).

The measurement of the specimen`s thickness for both SHPB and gas-gun experiments was made by the following equations (3.6) and (3.7), respectively:

$$L_{s\_SHPB} = (x_{final} + l_{sleeve} + 2l_{step\_ring}) - (l_{up} + l_{bp}) \quad (3.6)$$

$$L_{s\_Gas-gun} = (x_{final} + l_{ring} + l_{tube}) - l_{up} \quad (3.7)$$

where l_{step_ring}, l_{up}, l_{bp} are the length of the steppers ring, upper punch and bottom punch, respectively. x_{final} is measured by a caliper after to compress the specimen, as shown in Figure 3.2 and Figure 3.3.

3.3. Modified SHPB apparatus

In order to characterize the WC-Ni powder under compression, the specimen is confined in a sleeve and sandwiched between the incident and transmitter bars as is illustrated in Figure 3.4. Both bars are made of Inconel 718 alloy with a diameter of 12.7 mm, a length of 500 mm. The main properties of this Ni alloy are summarized in Table 3.4. The sound speed, C_b, was evaluated by applying the equation (2.4).

The striker bar was also made of Inconel 718 and had the same diameter value and a length of 230 mm. The incident and transmitter gauges are located equidistant from the specimen in the axial direction. A distance of 250 mm was selected to avoid the overlap in time of both incident and transmitted waves. In the rear of the incident bar, a pulse shaper was glued with the aim of eliminate the dispersion of the recorded signal.

Table 3.4. Inconel 718 properties (Special Metals, 2007).

$\rho_b(kg/m^3)$	$E_b(GPa)$	$C_b(m/s)$
8193	200	4940

The confining sleeve has an inner diameter of 12.78 mm which allows a clearance of 40 μm for the incident and transmitter bar sliding freely inside the sleeve. The friction between these bars was considering neglected.

The momentum bar was not employed in this setup because there are some reflection waves between momentum-transmitter bar interface which will unsettle the strain gauges signal for long time measurements that is required in this experiment for the wave velocity study.

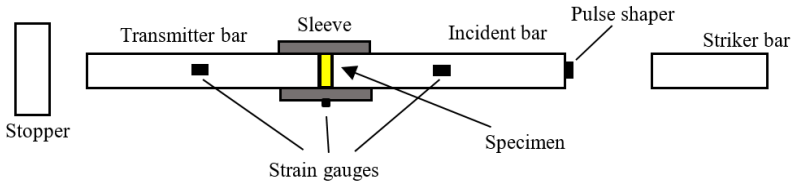

Figure 3.4. Modified SHPB setup for granular materials.

A strain gauge is placed on the outer surface of the sleeve in the hoop direction, as illustrated in Figure 3.5. The hoop strain gauge allows the deduction of the radial stress in the specimen during the compaction.

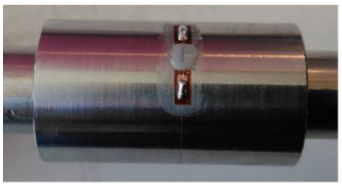

Figure 3.5. Hoop strain gauge placed in the sleeve.

The experimental tests were performed for three different specimen`s thickness and for three impact velocities. The intention is to study the influence of the thickness and the impact velocity of the striker bar, in the stress-strain state, (σ-ε), and sound speed, (C_S), in the WC-9Ni powder.

3.3.1. Method to determinate axial stress and strain

In order to apply the compression SHPB theory (section 2.1.1.) it is necessary to find a relation between the voltage, $V(t)$, from the bars strain gauges and the incident, reflected and transmitted waves ($\varepsilon_i(t),\ \varepsilon_r(t),\ \varepsilon_t(t)$). The method presented below was reported by Bo (2014). Subsequently, the SHPB configuration illustrated in Figure 3.6 was used to perform the calibration of incident and transmitter gauges. The momentum bar is used to absorb the rest of the compressive wave that comes from the calibrated bar (incident or transmitter bar).

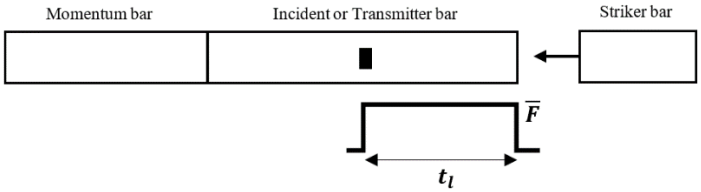

Figure 3.6. SHPB configuration for incident and transmitter gauges' calibration.

Knowing that the impedance, Z, which is the ratio between force, $\overline{F}$, and particle velocity, *w*, the following equation (3.8) is obtained for striker, transmitter and incident bars. This approach is valid since the components are made of the same material and the same cross-sectional area:

$$Z_b = Z_{sb} = \frac{\overline{F}}{w} = -\frac{A_b \times E_b}{C_b} \tag{3.8}$$

Replacing the variable E_b from the equation (2.4) into equation (3.8), the bars impedance can be written as follow:

$$Z_b = Z_{sb} = \rho_b A_b C_b \tag{3.9}$$

where ρ_b is the bars density.

When the striker bar hits the calibrated bar, the longitudinal load pulse developed at the interface has a constant value of force, $\overline{F}$, and duration $t_l = 2L_{sb}/C_b$, where L_{sb}

is the striker bar length. The particle velocity in the calibrated bar after the impact is half of the striker bar velocity, v_{sb}, resulting in the equation (3.10).

$$v_{sb} \times t_l = \frac{Z_b + Z_{sb}}{Z_b Z_{sb}} \times \overline{F} t_l \tag{3.10}$$

It is assumed that the momentum is conserved along the incident bar, $\overline{F} t_l$, which means that the force experienced at the gauge is the same as the one experienced at the interface of the striker-calibrated bar. Knowing that $C_{sb} = 2L_{sb}/t_l$, it can be substituted in equation (3.9) to express the impedance by $Z_{sb} = 2m_{sb}/t_l$, which when replaced in equation (3.10), a relation of average force and pulse duration can be described by the following equation:

$$\overline{F} = \frac{2m_{sb} \times v_{sb}}{\frac{2m_{sb}}{Z_b} + t_l} \tag{3.11}$$

where m_{sb} is the striker bar mass. The pulse duration, t_l, can also be approximated by integrating the voltage values recorded at the gauge, divided by the average voltage, $\overline{V}$, during the pulse wave, as illustrated in Figure 3.7. Thus, could be deduced by equation (3.12).

$$t_l = \frac{1}{\overline{V}} \int_{t_1}^{t_2} V(t) dt. \tag{3.12}$$

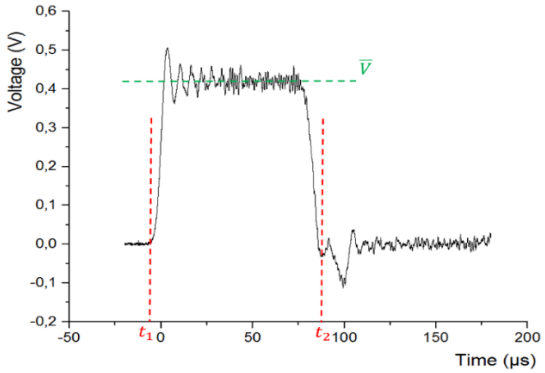

Figure 3.7. Incident pulse obtained in a calibrated bar.

The force, $F(t)$, developed in the calibrated bar can then be calibrated against the voltage, $V(t)$, thus obtaining the calibrated equation:

$$F(t) = k_1 V(t)[1 + k_2 V(t)] \tag{3.13}$$

where k_1 and k_2 are coefficients obtained for the calibration of incident and transmitter strain gauges, for a range of impact velocities. This calibration was made for a range of 60 shots at 5 different impact velocities, for each bar, wherein a linear fit of $\overline{F}(t)/\overline{V}$ versus $\overline{V}$ was obtained. Thus, the equation (3.13) can be written for incident and transmitter bars, as, respectively:

$$F_{inc}(t) = k_{1\_inc} V(t)\left[1 + k_{2\_inc} V(t)\right] \tag{3.14}$$

$$F_{tran}(t) = k_{1\_tran} V(t)\left[1 + k_{2\_tran} V(t)\right] \tag{3.15}$$

Applying the Hook`s law, the three waves, incident, reflected and transmitted can be obtained by:

$$\varepsilon_i(t) = \frac{k_{1\_inc} V_i(t)\left[1 + k_{2\_inc} V_i(t)\right]}{E_b A_b} \tag{3.16}$$

$$\varepsilon_r(t) = \frac{k_{1\_inc} V_r(t)\left[1 + k_{2\_inc} V_r(t)\right]}{E_b A_b} \tag{3.17}$$

$$\varepsilon_t(t) = \frac{k_{1\_tran} V_t(t)\left[1 + k_{2\_tran} V_t(t)\right]}{E_b A_b} \tag{3.18}$$

Subsequently, using equation (2.13), the axial strain can be determined in the specimen. Regarding the axial stress, equations (2.18) and/or (2.17) can be used with the difference that the specimen cross section area remains constant during the dynamic loading.

3.3.2. Method to determine radial stress

Figure 3.8 illustrates, schematically, the stresses involved in the specimen. The radial strain in the material will be considering neglected because the axial strain is significantly higher than the radial strain and the sleeve remains in elastic regime during the tests. Thus, the strain state of the specimen can be considered one-dimensional and the stress state bi-axial, with the following components of stress and strain tensors, that is:

$$\sigma_1 = \sigma_s;\ \sigma_2 = \sigma_3 = \sigma_r;\ \varepsilon_1 = \varepsilon_s;\ \varepsilon_2 = \varepsilon_3 = \varepsilon_r = 0 \tag{3.19}$$

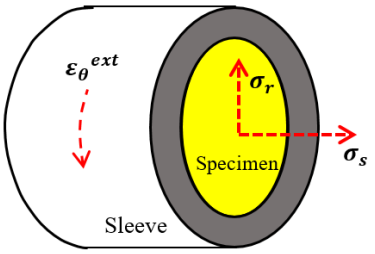

Figure 3.8. Stress state in the specimen confined by the sleeve.

To determinate de radial stress, σ_r, the thick-walled theory is used. For this reason, it is important that the sleeve has only elastic strain, which means that the yield stress is not achieved. The radial stress in the specimen can be related with the external hoop strain in the sleeve, $\varepsilon_\theta{}^{ext}$, by the following equation:

$$\sigma_r = \frac{E_{sleeve}}{2 \times {R_i}^2}\left({R_e}^2 - {R_i}^2\right){\varepsilon_\theta}^{ext}. \tag{3.20}$$

The relation between, ${\varepsilon_\theta}^{ext}$, and the signal recorded by the hoop strain gauge, V_θ, during the SHPB compression tests, is determined in section 3.3.3. The hydrostatic pressure in the specimen can be correlated to equation (3.21).

$$P_{hydr} = \frac{(\sigma_s + 2\sigma_r)}{3}. \tag{3.21}$$

3.3.3. Hoop strain gauge`s calibration

To determinate a relation between the signal recorded by the hoop strain gauge, V_θ, placed in the outer surface of the sleeve and the external hoop strain in the sleeve, ${\varepsilon_\theta}^{ext}$, a calibration setup was performed on the Instron machine, where the sleeve is compressed in the radial direction and the hoop strain gauge is positioned perpendicularly to the direction of the compression as illustrated in Figure 3.9.

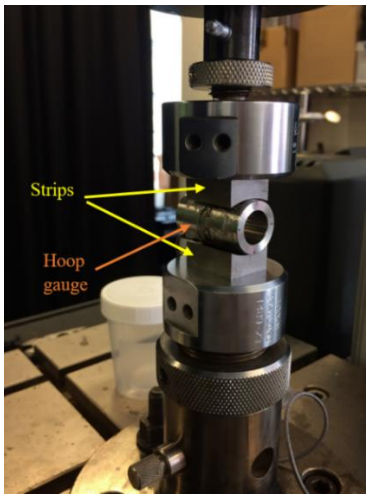

Figure 3.9. Calibration setup for hoop strain gauge.

From this calibration setup, a range of forces, F, is applied by the Instron machine and the hoop strain gauge signal is recorded by the oscilloscope. In Figure 3.10, is shown an example of a recorded signal when applied a force of 4718 N, wherein the average voltage, $\overline{V}$, is defined for each applied force.

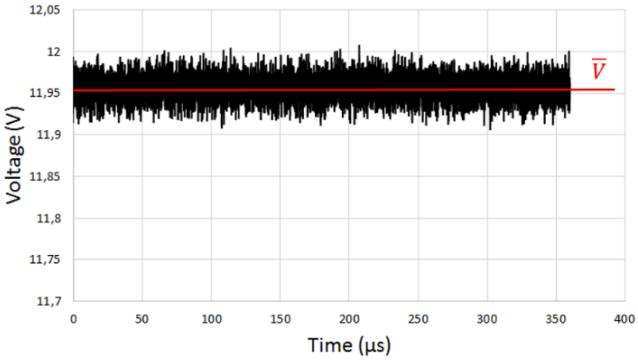

Figure 3.10. Recorded signal for a force of 4718 N.

Subsequently, the data ($\overline{V} - F$) were plotted in Figure 3.11 and a linear equation was used to approximate this relation. The standard deviation for each recorded signal is also presented.

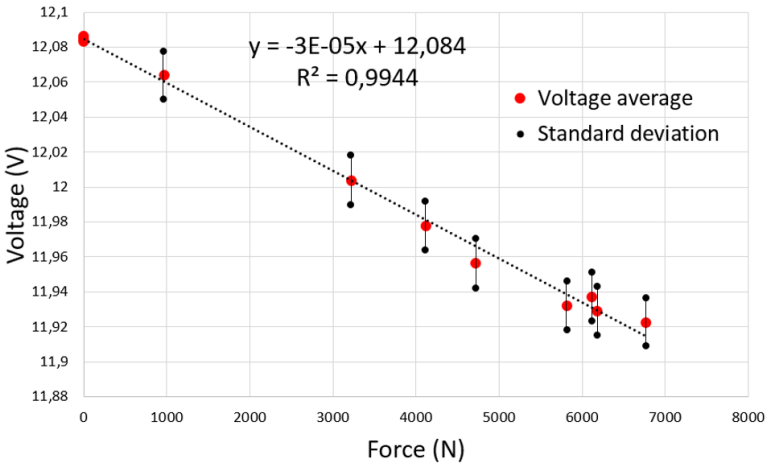

Figure 3.11. Hoop strain gauge calibration data.

It is important to notice that the oscilloscope showed an offset of 12.085 V, which is necessary to setup to zero. The SHPB compression tests, the oscilloscope was also setup to zero at the tests beginning.

Thus, the linear equation, which relates the force and the hoop strain gauge signal, is given by the following equation:

$$\overline{V} = -3 \times 10^{-5} F. \tag{3.22}$$

Assuming that this approach is a two-dimensional elasticity, that is, the distribution of stresses do not change along the length of the sleeve where the compression force is applied, the configuration could be estimated by two equal forces acting along the diameter of a circular ring, as exemplified in Figure 3.12.

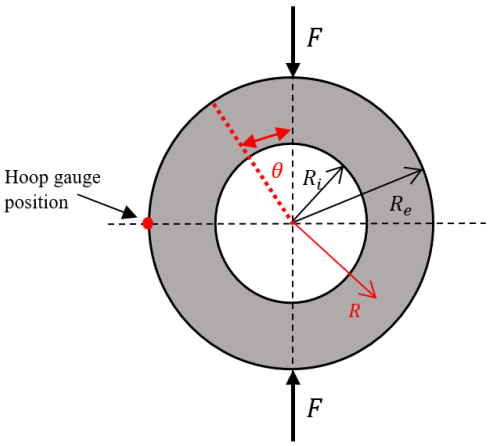

Figure 3.12. Theoretical approach for the calibration setup.

Chianese and Erdlac (1988) developed an analytical solution for the distribution of stresses in this configuration, thus, allowing a relation between the force, F, and the hoop stress, σ_θ, in any point of the ring. This general solution is given by equation (3.23).

$$\sigma_\theta = \frac{2F}{\pi R_e \times L_{strip}} K \tag{3.23}$$

where L_{strip} is the length of the strips that are in contact with the sleeve, and K is the stress concentration factor, which in this case is 6.85. ANNEX A can be consulted to determine the stress concentration factor.

Finally, relating equations (3.23) and (3.22), the relation between the signal recorded by the hoop strain gauge, V_θ, placed in the outer surface of the sleeve and the external hoop strain in the sleeve, ${\varepsilon_\theta}^{ext}$, can be describe by the following equation:

$$\begin{cases} \overline{V} = -3 \times 10^{-5} F \\ {\varepsilon_\theta}^{ext} = \dfrac{2F}{\pi R_e \times L_{strip} \times E_{sleeve}} \times \mathrm{K} \end{cases} \Rightarrow {\varepsilon_\theta}^{ext} = \frac{\frac{2}{-3 \times 10^{-5}} V_\theta}{\pi R_e \times L_{strip} \times E_{sleeve}} \times \mathrm{K} \quad (3.24)$$

3.3.4. Sound speed analysis

The sound speed in the specimen, C_s, was determined for the first compression wave by the following equation:

$$C_s = \frac{L_s}{\Delta t_t} \quad (3.25)$$

where Δt_t is the time that the longitudinal wave takes to travel along the specimen`s thickness. It can be determined as:

$$\Delta t_t = \Delta t_s - \Delta t_{blank} \quad (3.26)$$

where Δt_s and Δt_{blank} are the interval of time between the first signal of the transmitted and incident wave, for a test with specimen and without specimen, respectively. The SHPB configuration for sound speed evaluation is illustrated in Figure 3.13.

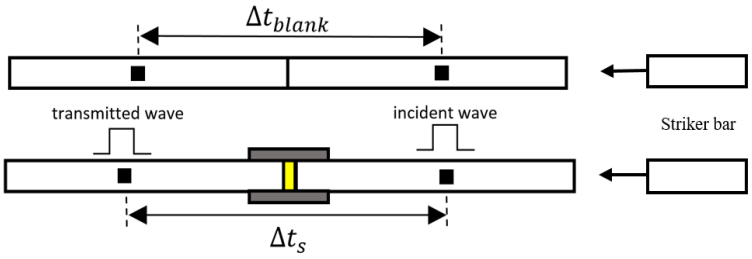

Figure 3.13. SHPB configuration for sound speed evaluation.

The sound speed in the bars does not depend of impact velocity of striker bar, and for this reason the interval of time, Δt_{blank}, was assumed to be the same for different impact velocities. Thus, only one impact velocity was used to calculate Δt_{blank} and the recorded signals are presented in Figure 3.14 for incident and transmitter gauge.

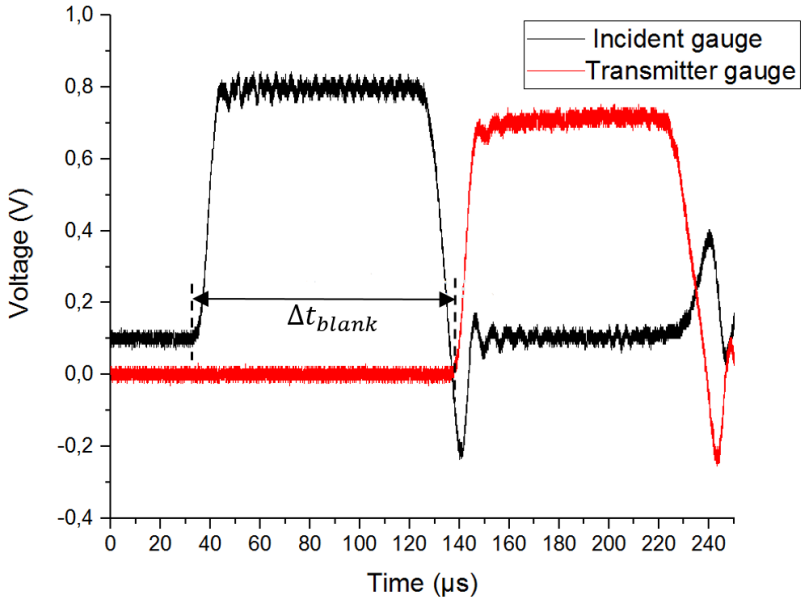

Figure 3.14. Recorded signals for test without specimen.

3.3.5. Variation of sound speed analysis for multiple loading

In the compression SHPB test, the specimen is compressed more than once for a range of longitudinal waves (multiple loading), which means that the relative density of the specimen increases and, consequently, it affects the sound speed for each compression wave until it reaches the stability. This behaviour can be identified by the increase in the amplitude of the transmitted waves for a constant incident wave amplitude over a long period of time, as reported by Choudhury (2016).

Wherefore, it is necessary to take into account with the attenuation of the waves in the bars, so that the transmitted waves only identify the behaviour of the specimen.

To obtain the waves attenuation in both incident and transmitter bars, the SHPB configuration clarified in Figure 3.15 was used. It is important to mention the gap occurrence between the bar and the stopper, which allows a free reverberation of the wave before the bar hits the stopper.

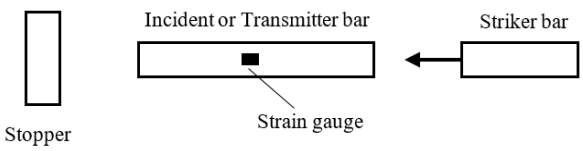

Figure 3.15. SHPB configuration for bars` attenuation.

Figure 3.16 presents an example of the wave signal obtain using this SHPB configuration. As can be concluded, there is a decay of the waves with time.

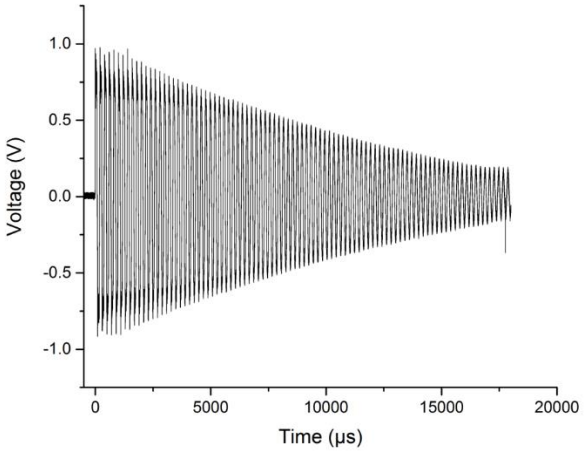

Figure 3.16. Example of attenuation wave in a metallic bar.

To compensate the decay, the following exponential function can be used to approximate it:

$$y(t) = c_0 + c_1 e^{c_2 t} \tag{3.27}$$

where c_0, c_1 and c_2 are the fitting coefficients, for a given impact velocity. Subsequently, with a linear interpolation/ extrapolation the decay of the waves in the bars can be estimated for a desire impact velocity of the striker bar. Dividing the peak of the first wave amplitude in the bars, V_1, by the equation (3.27), a scaling factor, $\gamma(t)$, is obtained, that is:

$$\gamma(t) = \frac{V_1}{c_0 + c_1 e^{c_2 t}}. \tag{3.28}$$

Multiplying the scaling factor by both incident and transmitter gauge signals for the SHPB specimen's tests, a scaled signal which compensate the attenuation in the bars can be obtained. The expression is the (3.29).

$$V^{scaled}(t) = \gamma(t) \times V(t). \tag{3.29}$$

3.4. Multiple target for gas-gun experiments

In this section the setup concerning the multiple target setup is presented. The proposal was to study the shock compaction behavior of WC-9Ni powders for the single stage gas gun with 50mm bore. The target, as exemplified in Figure 3.17, was specially designed to hold 3 specimens with a diameter of 12.1 mm, wherein the shock loading is studied. The main advantage of this setup is possibility of study, at the same time, different specimens including different composition and particle size, dissimilar initial density and also unlike initial length.

The projectile, which is composed by a polymeric (PMMA) sabot and a metallic (W) flier, was launched by the gas gun to hit the target. The copper (Cu) driver was hold by a precision kinematic mirror mount with 76.2mm (3``) of diameter, which allows to align the target perfectly planar to the projectile. The 3 specimens, that were first preloaded inside the rings, were placed in front of the cooper driver where the rings are hold by a polymer holder. The PMMA windows, placed in front of the specimens, were hold by another PMMA holder. The bolts were connected to the PMMA and polymer holders to press these against the Cu driver.

The 2D drawings of the target setup can be consulted in ANNEX C – 2D drawings of the multiple target setup.

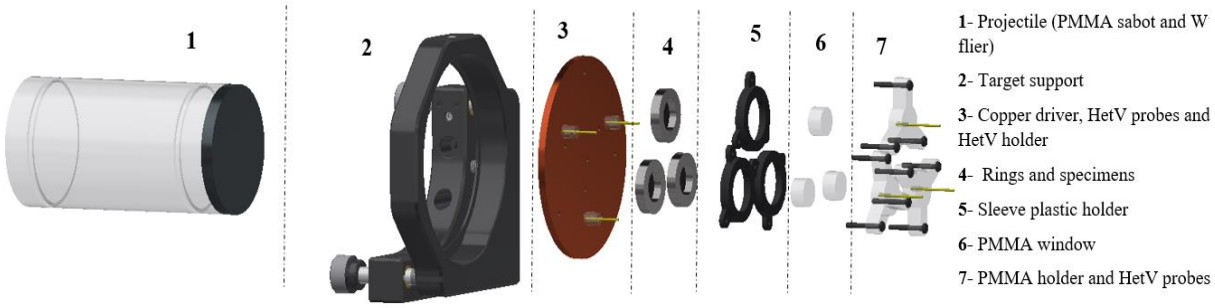

Figure 3.17. Target setup - exploded view.

3.4.1. Experimental Methods

In order to study the shock loading, the specimens were placed between the Cu driver and a PMMA window. The mounting scheme is illustrated in Figure 3.18.

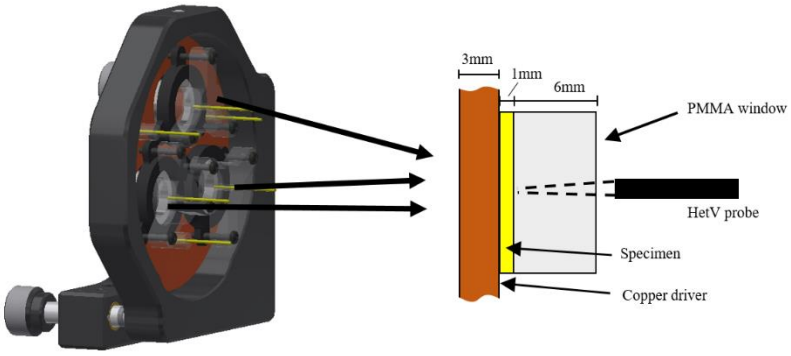

Figure 3.18. Target setup with the specimens' configuration.

This experimental setup allows to measure the particle velocity, u_p, and to deduce the shock wave velocity of the powder, U_s.

The particle velocity is directly obtained by Heterodyne Velocimetry (HetV) technique where the HetV probes was placed in the PMMA holder that picks up the particle velocity of the interface between PMMA window and specimen. Three HetV probes were also placed in the Cu driver that picks up the arrival time of the shock wave at the specimen. The shock wave velocity was derived from the distance travelled by the wave inside the specimen within a span time. During the measurement time it was necessary to keep a steady shock wave and because of that it is important to take account with release waves from the rear of the W flier as well as from the edges of the specimen and Cu driver.

3.4.2. Brief description of data analysis

In order to determine the Hugoniot curves $(P - v)$ and $(P - u_p)$ of the WC-9Ni powder, two ways can be taken to calculate the particle velocity, u_p: from the measurement of the particle velocity obtained by the HetV probes, or using the impedance matching techniques, as shown in Figure 3.19, with the known properties of the W flier and the Cu driver. Both materials can be described by elastic-perfectly-plastic strength model where they have elastic and plastic regimes as reported by Vogler (2005).

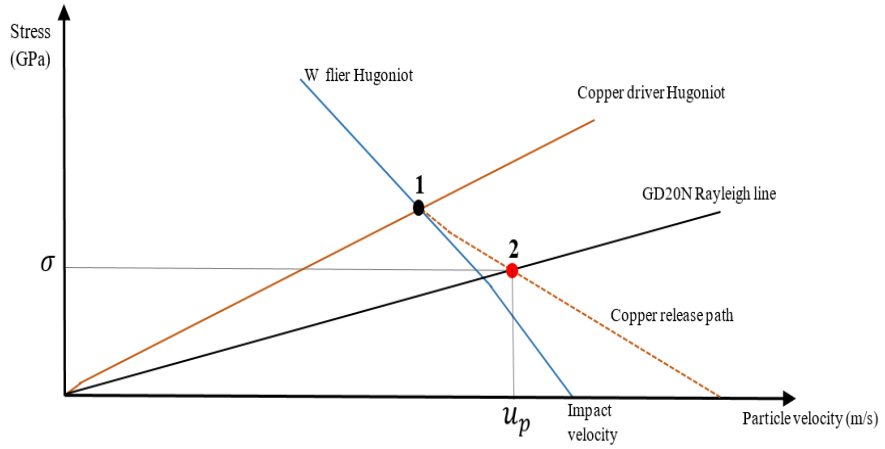

Figure 3.19. Impedance matching technique.

The Hugoniot curve $(P - u_p)$ of the W flier that hits the copper driver with an impact velocity, V_{impact}, can be related by the following equations for the elastic and the plastic regimes respectively:

$$\sigma^E = \rho_0 c_L \left(u_p - V_{impact}\right) \tag{3.30}$$

$$\sigma_n = \rho_0 \left(a + b\left(u_p - V_{impact}\right)\right)\left(u_p - V_{impact}\right) + \frac{2}{3}Y. \tag{3.31}$$

The Hugoniot of the copper driver for the elastic and plastic regimes can be related directly from the equations (2.28) and (2.29), respectively, because before the shock the copper driver is at rest ($u_0 = 0$). The material properties ρ_0, a, b, $Y$and c_L for both materials can be consulted in Table 3.5. The shock state of these materials is given by the intersection (point 1) of blue and orange lines, as shown in Figure 3.19. When the shock across the copper driver and reaches the powder, it releases to the Hugoniot of the powder. The state shock in the powder (point 2) can be found by the intersection of the release path of the copper, that can be described by the unloading path as show in Figure 2.8, and the Rayleigh line of the powder that is given by the following equation:

$$p = \rho_0 U_s u_p \tag{3.32}$$

where ρ_0 is the initial density of the specimen determined in section 3.2.3, and U_s is the shock wave velocity derived using the HetV probes.

By applying this equation, the particle velocity u_p, and the stress p of the powder can be derived for a given impact velocity. Following the same procedure for different impact velocities, the Hugoniot curves for the WC-Ni powder were obtained.

Table 3.5. The main properties (Ron, 2009).

	Material	
Material Properties	Cu	W
ρ_0 (g/cm^3)	8.93	19.22
a (mm/μs)	3.94	4.03
b	1.49	1.24
c_L(mm/μs)	4.76	5.22
$v_H(cm^3/g)$	0.111	0.051
u_H (mm/μs)	0.0047	0.039
$\sigma_H(GPa)$	0.2	3.9
$Y(GPa)$	0.096	2.374

4. RESULTS AND DISCUSSION

4.1. INSTRON preloading specimens

A force of 9 kN was applied, using a INTRON machine, in order to get the same relative density in all specimens. A total of five samples were used. The preloading characteristics of each specimen are summarised in the Table 4.1.

Table 4.1. Preloading characteristics of the five WC-9Ni samples

Specimen	Mass (g)	$L_s(mm)$	$\rho_s(g/cm^3)$	RD (%)
#1	4.52	4.98	7.06	48.13
#2	4.52	4.85	7.25	49.38
#3	4.52	4.87	7.23	49.20
#4	3.39	3.65	7.24	49.31
#5	2.26	2.44	7.21	49.04

As can be concluded from the analysis of the Table 4.1, the thickness of *#1*, *#2* and *#3* specimens has approximately the same value. The idea is to evaluate the impact velocity changing effect. On the other hand, the specimens *#3*, *#4* and *#5* were used to study the influence of thickness change for the same impact velocity.

4.2. Dynamic response of WC-Ni powder

After pre-compress the powders, for a relative density of ≅ 49%, the experimental work begins by using the modified SHPB setup, as shown in Figure 3.4. Three impact velocities, of 16.1, 18, and 19.4 m/s were selected, as depicted in Table 4.2.

Table 4.2. Impact velocity of the striker bar for each specimen

Impact velocity of striker bar		
16.1 m/s	**18 m/s**	**19.4 m/s**
#1	*#2*	*#3*
-	-	*#4*
-	-	*#5*

The average strain rate obtained for each specimen is summarised in Table 4.3. This property was calculated by applying equation (2.12) as the mean value between the time corresponding 10μs and 100μs. As can be concluded from the experimental results, the strain rate increases with the increases of the impact velocity (specimens #1 to #3), as was expected, and slight increase for lower specimens` thickness (specimens #3 to 5#).

Table 4.3. Average strain rate for each specimen.

Specimen	**Strain rate** (s^{-1})
#1	1639
#2	1850
#3	2004
#4	2046
#5	2071

Figure 4.1 presents the results for the specimen #1. The evolutions obtained for the other specimens, #2 to #5, are shown in Figure 4.2 to Figure 4.5, respectively.

The signals recorded by the three strain gauges are depicted in Figure 4.1a), wherein can be observed the four waves used to analyse the dynamic response of the WC-Ni powder for the first compression wave, as explained previously in section 3.3.

As can be seen in Figure 4.1b), the strains are derived from the four waves, shifted in time for the first dynamic loading, wherein the time of the waves propagation in the bars is removed, and consequently, incident and reflected strains are settle to 0 in time. Transmitted and hoop strains have a delay that is associated with the time of the wave propagation in the specimen, Δt_t, where the hoop strain has a delay that is approximately half the transmitted strain delay.

Some problems emerged during the data analysis of the experimental results. Despite of the length of the striker bar be smaller than the distance between incident gauge and specimen-incident bar interface, there is an overlapping of the incident and transmitted waves, that does not allow to deduce a correct response of the specimen using the incident gauge, during the rising and falling time of the incident wave. The time of overlapping that is approximately 10μs at the beginning and end of the first dynamic loading, can be observed in Figure 4.1b), where both waves should start and ends at 0 strain but it does not happen.

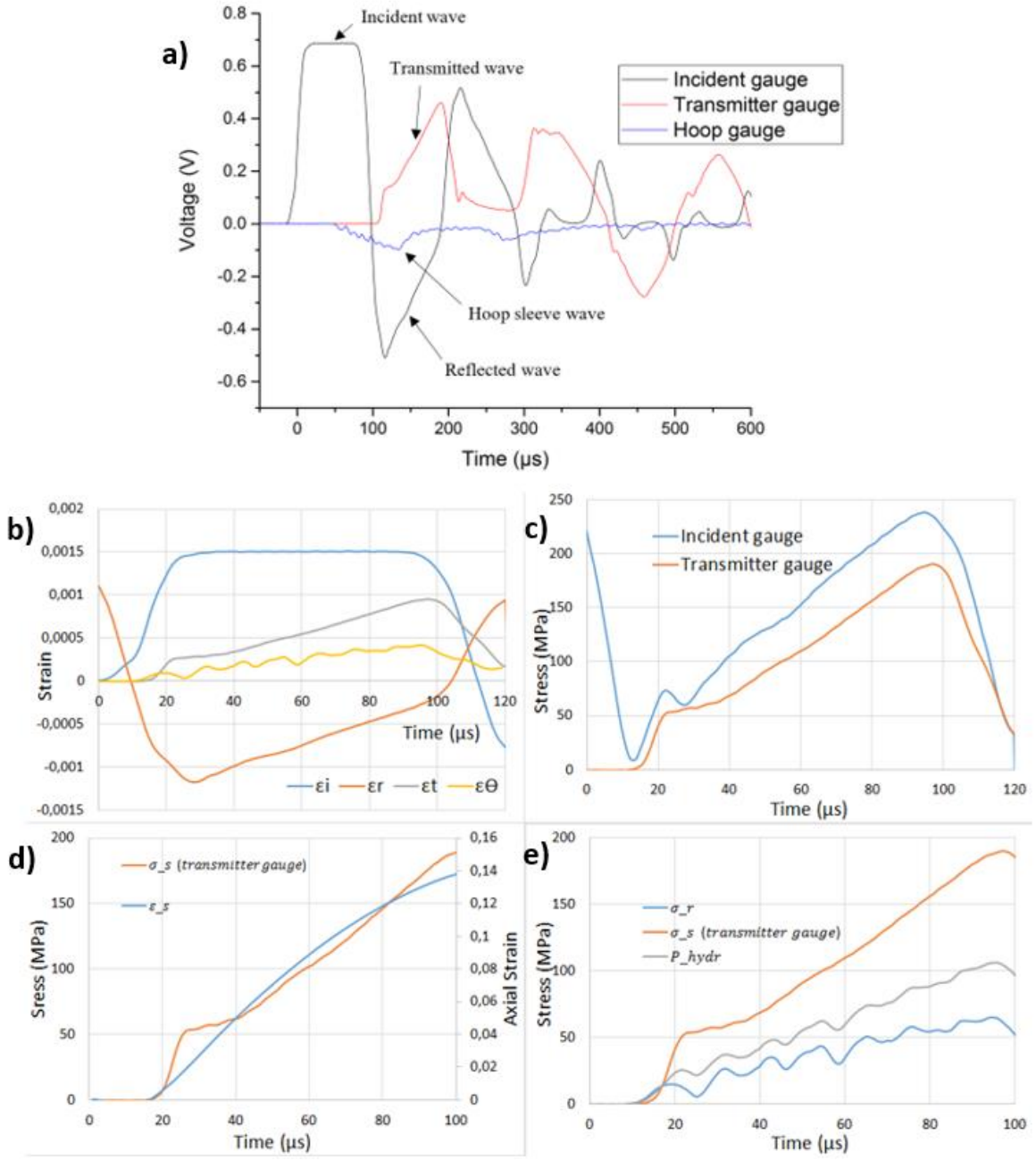

Figure 4.1. Results for specimen #1: a) Signals recorded by the 3 strain gauges; b) Strains shifted in time; c) Axial stress derived from incident and transmitter gauges; d) Axial stress and strain versus time; e) Stress states versus time.

The overlapping behavior might be attributed to the pulse shaper that increase the rising and falling time of incident wave and, consequently, the pulse duration rises. Another point that should be focused concerning Figure 4.1a), is the dispersion of the hoop sleeve wave. This could be due to noise which is easily picked up because of the lower

amplitude of the signal recorded by the hoop sleeve gauge. This dispersion obtaining make difficult the response powder analysis in the radial direction.

Figure 4.1c), presents the axial stress evolution deduced from the incident and transmitter gauges, two and one wave analysis, respectively. The stress deduced by the incident gauge shows an initial spike that could be attributed to the time overlapping, as was explained above. For this reason, the stress states evaluations of the WC-9Ni specimens were done by using only the axial stress deduced from transmitter gauge. As can be also observed in Figure 4.1c), there is no equilibrium of the axial stresses in the specimen interfaces, meaning that the homogeneity of the stress fields during the dynamic loading was not achieved. This behaviour can be justified by the low sound speed velocity and the higher deformation in granular materials.

Figure 4.1d) exhibits the evolution of the axial stress and the strain as a function of time; while the evolution of the stress involved in the specimen (axial and radial stresses and hydrostatic pressure), wherein the radial stress is about 40% of the axial stress, is presented in Figure 4.1e).

It is important to highlight two phases during the dynamic compression of the WC-9Ni powder, noticed in Figure 4.1e). In the first phase, the axial stress increases sharply whereas the radial stress seems to remain very low; in the second phase the radial stress begins to increases and the axial stress increase slower than in the first phase. These powder behaviours can be more noticeable in specimens 3# and 5#, Figure 4.3 and Figure 4.5, wherein the noise in the hoop strain gauge signal is lower. The first phase seems to be similar to a uniaxial compression test wherein the specimen is not confined in the radial direction. One possible explanation is the powder dynamic response, that is, in the beginning of the dynamic loading the particles rearrangement can be easily done in the radial direction until the transition between these phases.

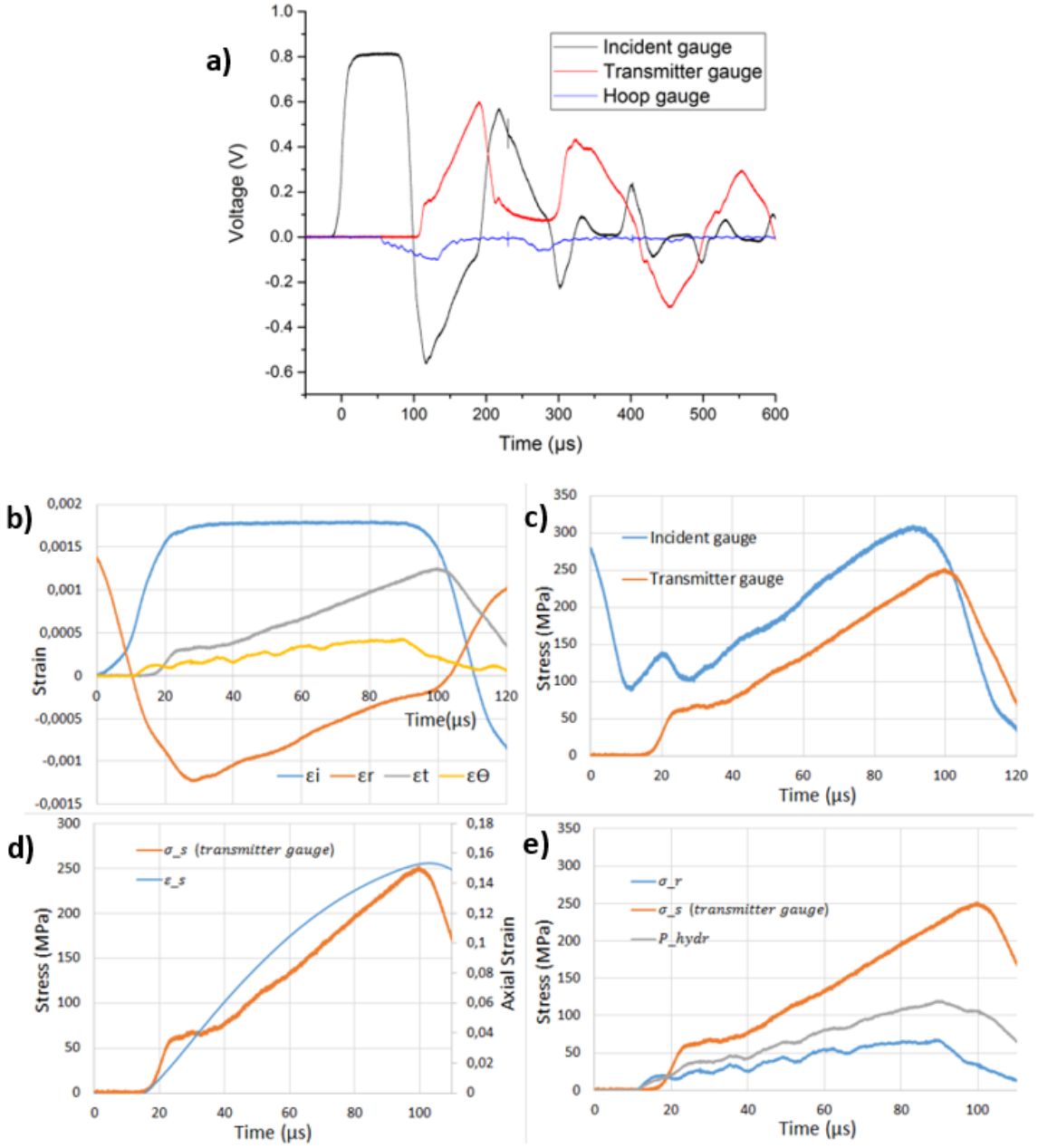

Figure 4.2. Results for specimen #2: a) Signal recorded by the 3 strain gauges; b) Strains shifted in time; c) Axial stress derived from incident and transmitter gauges; d) Axial stress and strain versus time; e) Stress state versus time.

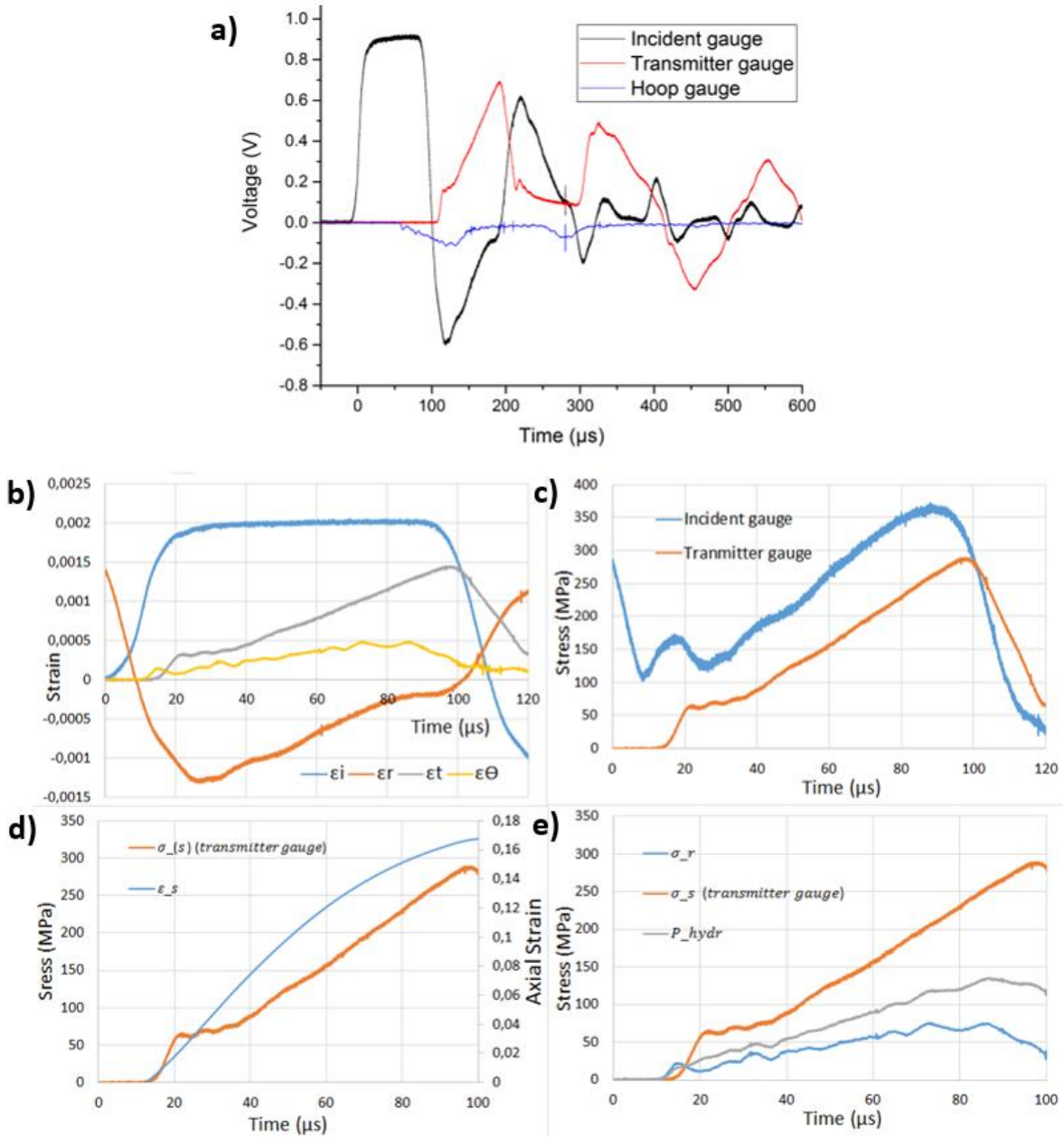

Figure 4.3. Results for specimen #3: a) Signal recorded by the 3 strain gauges; b) Strains shifted in time; c) Axial stress derived from incident and transmitter gauges; d) Axial stress and strain versus time; e) Stress state versus time.

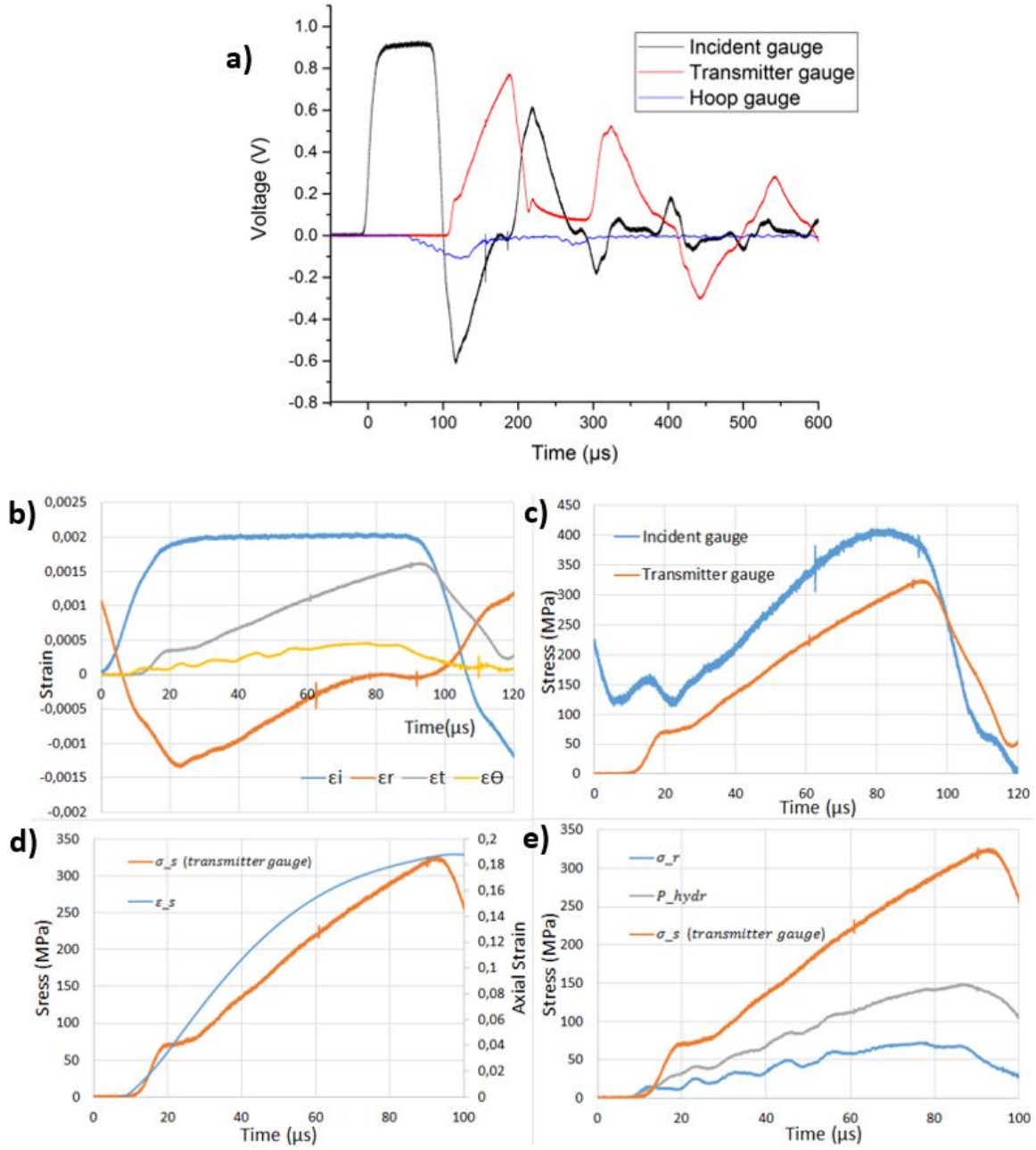

Figure 4.4. Results for specimen #4: a) Signal recorded by the 3 strain gauges; b) Strains shifted in time; c) Axial stress derived from incident and transmitter gauges; d) Axial stress and strain versus time; e) Stress state versus time.

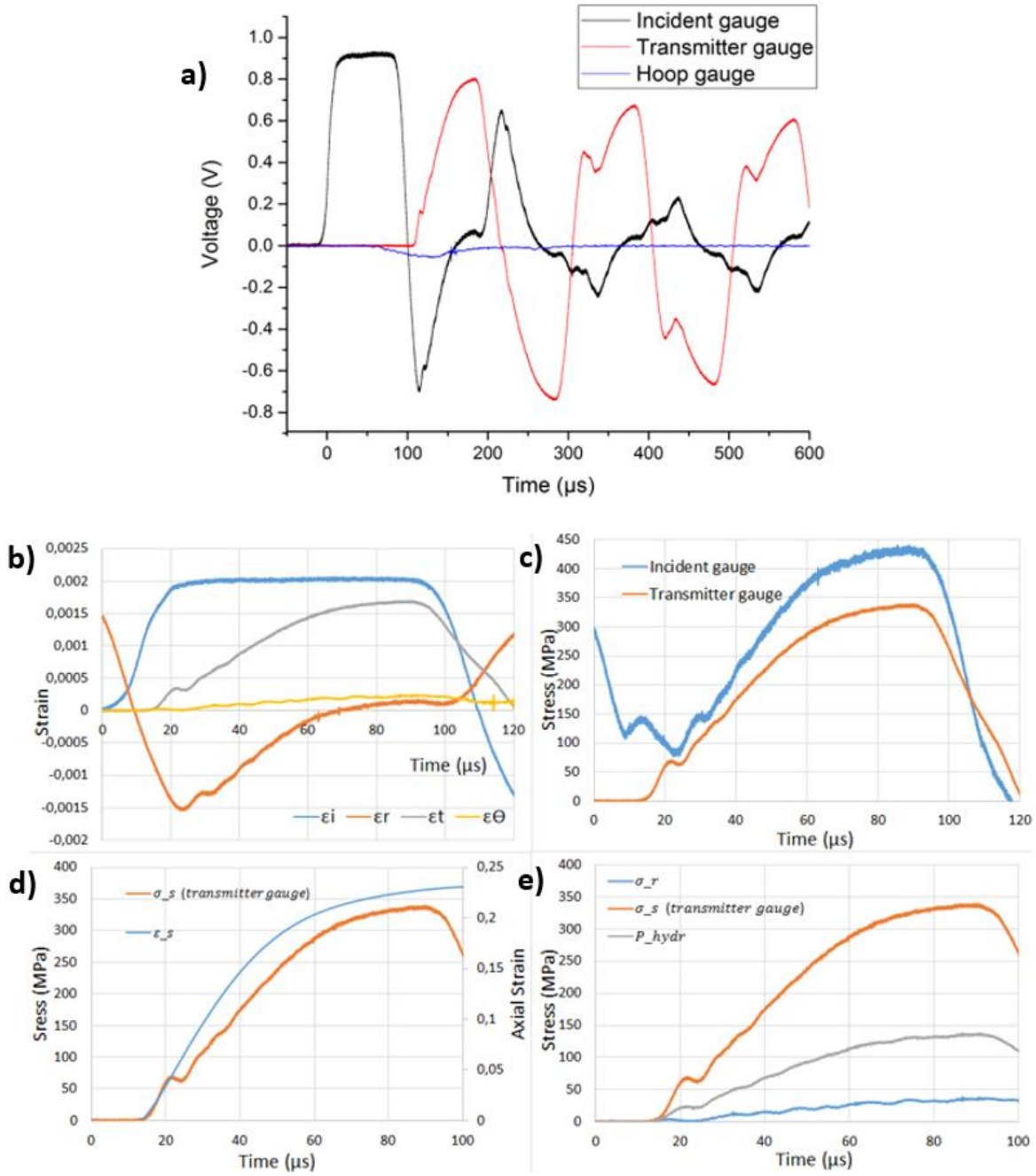

Figure 4.5. Results for specimen #5: a) Signal recorded by the 3 strain gauges; b) Strains shifted in time; c) Axial stress derived from incident and transmitter gauges; d) Axial stress and strain versus time; e) Stress state versus time.

4.2.1. Comparison between specimens

In this section the influence of thickness and impact velocity in the specimens is analysed. The variation of the ratio between stress output and input specimen`s interfaces as a function of time is presented in Figure 4.6. According to Figure 4.6a) the axial stress in both interfaces for specimen #1 (lower impact velocity) is closer than for the specimens #2

and #3 (higher impact velocity). This is due to the inertia which increases for higher impact velocities and consequently it acts as a resistance for the particles motion.

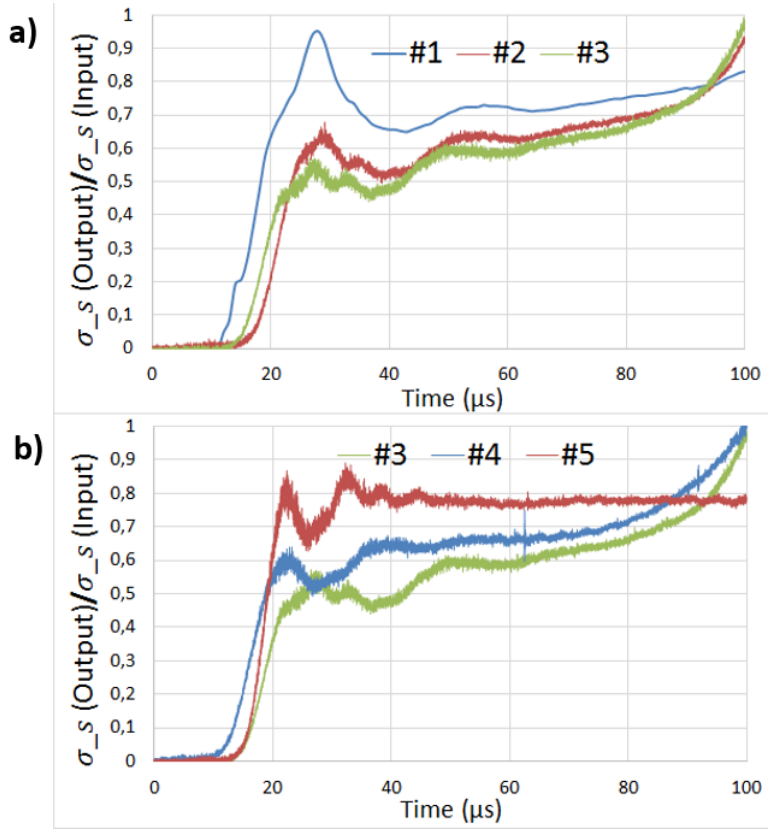

Figure 4.6. Ratio between stress in output and input specimen`s interfaces: a) Influence of impact velocity; b) Influence of thickness.

Regarding the influence of thickness, in Figure 4.6b) can be observed that for specimen #5 (lower thickness), the axial stress in both interfaces is closer than for the specimens #3 and #4 (higher thickness). The reason is that for lower thickness specimens there is more reverberations waves inside the powder that approximates the stress in both specimen`s interfaces.

Figure 4.7 shown the axial stress-strain curves. For different impact velocities, Figure 4.7a), the axial dynamic response of the specimens is very similar, with the only different that for specimen 3#, the maximum axial stress-strain achieved in the powder is higher for higher impact velocities, as expected. For different thickness, Figure 4.7b), there is a slight difference in the axial dynamic response, wherein for specimen 5#, the axial stress-strain curve is less sloping but the maximum axial stress-strain achieved is higher.

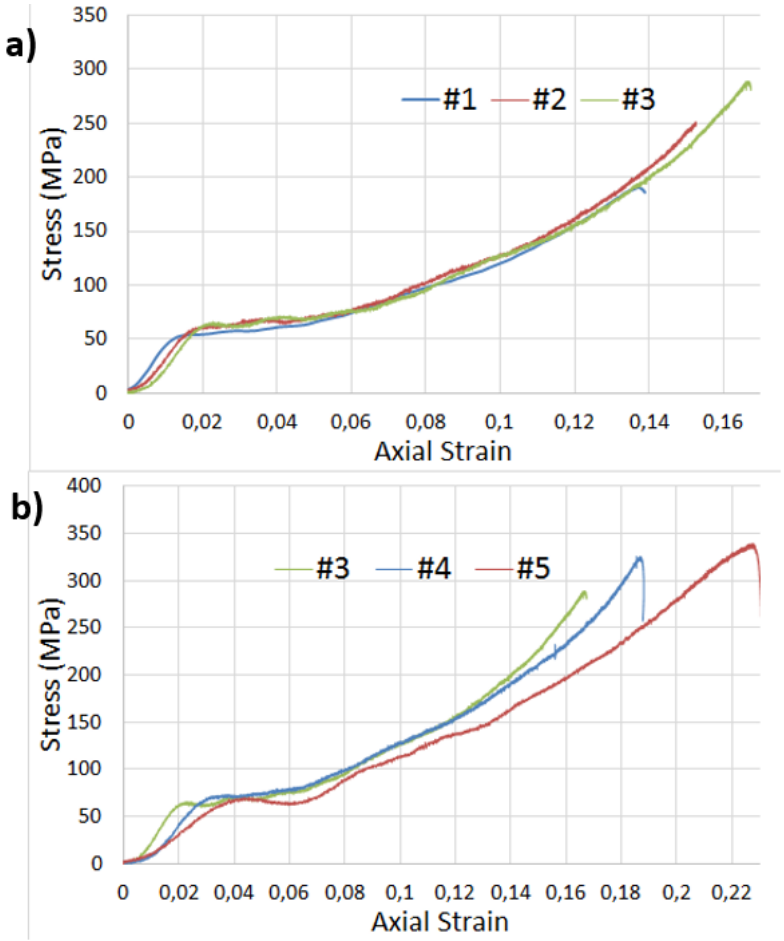

Figure 4.7. Axial stress-strain curves: a) Influence of impact velocity; b) Influence of thickness.

In Figure 4.8 the hydrostatic pressure response of the specimens is compared. Once again, there is not a noticeable influence of the impact velocity, Figure 4.8a), as seen for the axial stress-strain response. It indicates that dynamic response involved in the specimen does not depends of the impact velocity of the striker bar. For different thickness, the difference between hydrostatic pressure curves is higher than for axial stress-strain curves, which indicates that the radial stress for the specimen 5# is lower than for specimens 3# and 4#. It can be explained because specimen 5# has a thickness of 2.44 mm, which makes the specimen approximate from one-dimensional stress state.

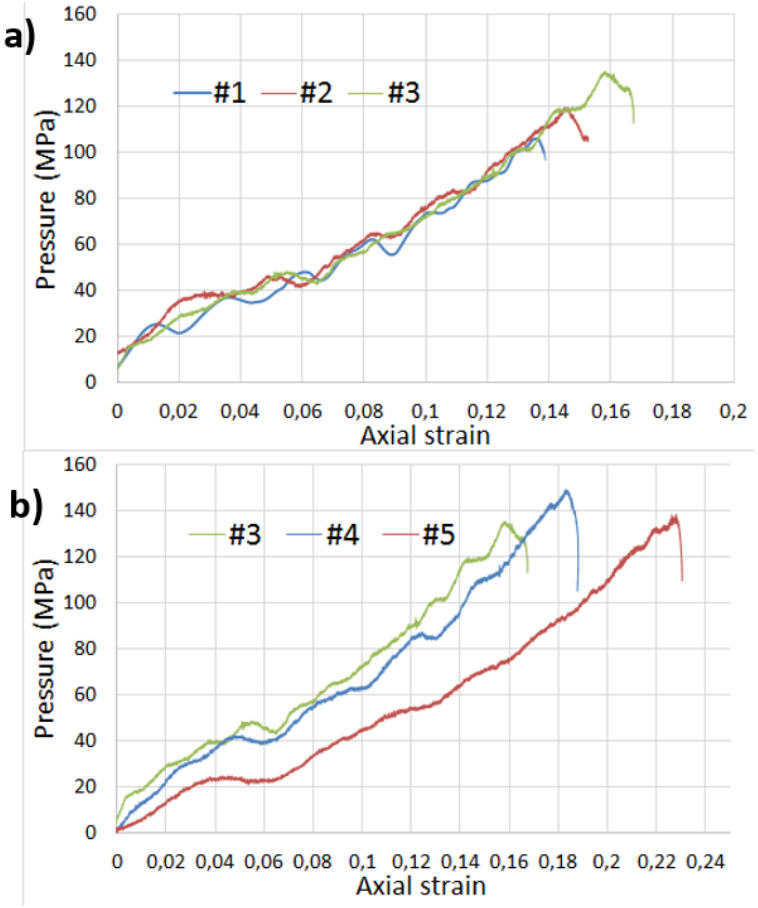

Figure 4.8. Hydrostatic pressure curves: a) Influence of impact velocity; b) Influence of thickness.

Table 4.4 presents the maximum stress and strain states as well as the relative density achieved for the first compressive wave (first incident wave) of the five samples.

Table 4.4. WC-Ni powder response for the first compressive wave

Specimen	Max. axial stress (MPa) (transmitter gauge)	Max. axial strain	Max. radial stress (MPa)	RD (%)
#1	190.47	0.141	65.05	55.36
#2	251.58	0.153	67.95	57.62
#3	289.26	0.167	75.78	58.18
#4	325.87	0.188	73.14	59.53
#5	339.60	0.231	39.18	61.78

4.2.2. Sound speed in the powder

Following the sound speed analysis as described in section 3.3.4, the intervals of time Δt_s and Δt_{blank}, were measured for the tests with specimen and the test without specimen, respectively, and are presented in Table 4.5.

Figure 4.9 shown the recorded signal for the specimen #1 where the interval of time that the waves takes from incident to transmitter gauges is depicted.

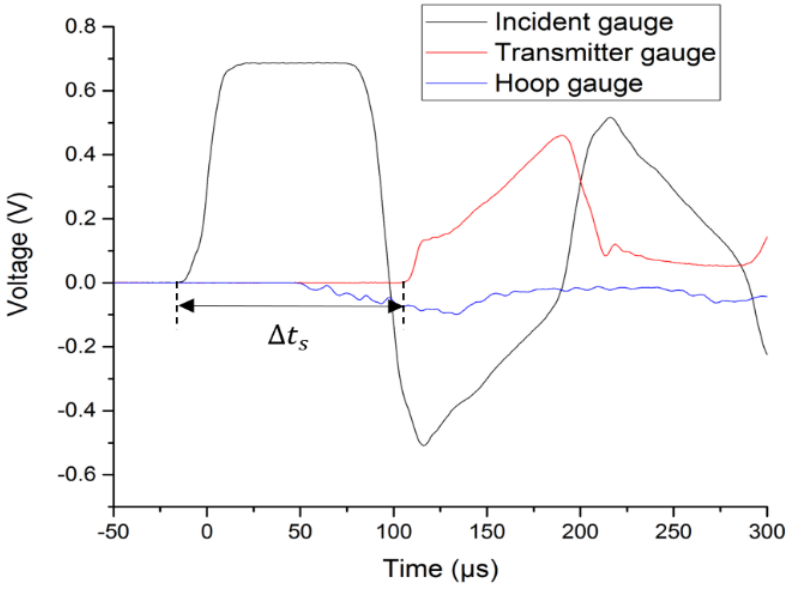

Figure 4.9. Recorded signals for specimen #1.

From the results presented in Table 4.6 one can concluded that the sound speed in the powder is very similar for the sound speed in the air, that is $\approx 343\ m/s$. These results are similar to those presented by Chevrier and Masseran (2016) and Choudhury (2016) who used sand as material. Some errors can be associated with the measurement of the specimens` thickness and the time that the waves takes to travel along the specimen.

Table 4.5. Sound speed in the WC-Ni specimens

Specimen	Δt_{blank} (μs)	Δt_s (μs)	$\Delta t_t = \Delta t_s - \Delta t_{blank}$	$C_s = \frac{L_s}{\Delta t_t}$ (m/s)
#1	104	120	16	≈311
#2		119	15	≈323
#3		117	13	≈374
#4		115	11	≈331
#5		117	13	≈187

The low values obtained for the sound speed can be attributed to the high level of the specimen`s porosity, ≅ 49%. Analysing Table 4.6 and assuming that the Young´s Modulus of WC-Ni solid material (E_{WC-Ni}) is 650 GPa, the ratio E_s/E_{WC-Ni} is approximately zero, which might explain the reason of low values of the sound speed in the powder.

Table 4.6. Young`s Modulus of the specimens

Specimen	$\rho_s(g/cm^3)$	$C_s\ (m/s)$	$E_s = C_s{}^2 \times \rho\ (MPa)$	E_s/E_{WC-Ni}
#1	7.06	≈311	≈680	≈0.001
#2	7.25	≈323	≈760	
#3	7.23	≈374	≈1000	
#4	7.24	≈331	≈790	
#5	7.21	≈187	≈250	≈0.0003

4.2.3. Variation of sound speed for multiple loading

Regarding the sound speed variation in the specimens, is not possible to use the SHPB modified setup for this purpose. As illustrated in Figure 4.10, after the second compression wave (incident wave) the hoop gauge does not record any wave.

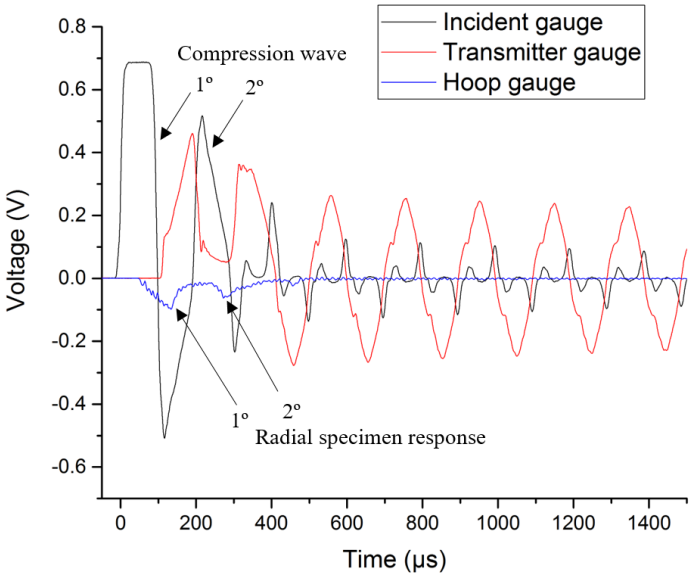

Figure 4.10. Recorded signals for specimen #1

This behavior suggests that the specimen is no more in contact with both incident and transmitter bars. One can also be observed that, after the second incident wave, the amplitude signal of the transmitted gauge is higher than that recorded by the incident gauge, which would not make sense if the specimen kept in contact with the bars. For this reason, the variation of sound speed for multiple loading cannot be applied to WC-9Ni powder.

5. CONCLUSIONS

In this work, WC-Ni powder, containing 9wt%Ni, was tested on SHPB apparatus by selecting different impact velocities and specimen`s thickness. The porosity degree of samples was 49%.

The results were used to obtain the dynamic response and sound speed of the WC-Ni powder at medium strain rates. A multiple target setup was also design to obtain the Hugoniot response of the WC-Ni powder using a gas gun to create a planar shock wave.

Regarding the SHPB apparatus, a first dynamic response at medium strain rates was obtained for WC-Ni powder, wherein two phases were identified during the compressive loading, although the causes of this behaviour were not well recognized. Another important conclusion is that the stress field is not homogeneous in the powder. A successful new method to deduce the radial stress in the specimen was developed, which is a very good point of this work. Moreover, some problems emerged on the SHPB analysis as described below:

1. Overlapping of the waves that are used to deduce the response of the powder;
2. The specimen remains only in contact with incident and transmitted bars during the first two compressive loadings, and consequently, does not allow to evaluate the variation of sound speed for multiple loadings;
3. Some dispersion in hoop strain gauge signal due to the low amplitude of the signal.

5.1. Recommendations for future work

This work should be extended in the future, not only for improvements on the SHPB apparatus, but also for the understanding of dynamic compaction in this powder for a wider range of strain rates. Regarding that, some recommendations are exposed below:

1. Using incident and transmitter longer bars or a shorter striker bar will solve the problem of incident-reflected overlapping;

2. Some modification on SHPB apparatus should be done in order to keep the specimen in contact with incident and transmitter bars for a longer period of time;
3. A glass sleeve might be a good solution to confine the specimens, and a high speed camera can be used to record the tests in order to see the particles compaction during the dynamic loading for a well understanding of the two phases identified. The glass sleeve can be also useful because the dispersion on the hoop strain gauge might be lower;
4. Some modification on SHPB apparatus should be done in order to recover the specimens and characterize them by SEM;
5. Another strain gauge could be placed in the sleeve in the hoop direction and the results of both hoop strain gauges' signals should me compared;
6. A method analysis should be developed to take account with friction between specimen and sleeve and to take account with inertia effects on the specimen;
7. Quasi-Static using a INSTRON machine, and planar impact tests using a gas gun with the target setup design in this work should be performed, in order to compare the response of this powder for an extended range of strain rates.

BIBLIOGRAPHY

Ayob, A. B., Tamin, M. N., Elbasheer, M. Kabashi (2009), "Pressure Limits of Thick-Walled Cylinders", Proceedings of the International MultiConference of Engineers and Computer Scientists, Vol II IMECS.

Bo, Chiara (2014), "Investigation of the effects of high pressure pulses on biological samples", Dissertation for the degree of Doctor of Philosophy, Imperial College London, Department of Physics.

Chevrier, Boris, Masseran, Thomas, (2016), "The shear behaviour of granular materials under dynamic loading", Imperial College, Blackett Laboratory, Institute of Shock Physics.

Chianese, R.B., Erdlac, R.J. (1988), "The general solution to the distribution of stresses in a circular ring compressed by two forces acting along a diameter." Q. J. Mechanics Appl. Math., 41(2), 239–247.

Choudhury, Danyal (2016), "An investigation of sound propagation in granular media", Master thesis project, Project code: ISP-Proud-3, Imperial College London, Department of Physics.

Forbes, Jerry W. (2012) "Shock wave compression of condensed matter", Springer Heidelberg New York Dordrecht London.

Forquin, P., Gary, G. Gatuingt, F. (2008), "A testing technique for concrete under confinement at high rates of strain", In: International Journal of Impact Engineering. 35(6):425-446.

Gama, Lopatnikov, Gillespie, Jr (2004), "Hopkinson bar experimental technique: A critical review", Appl Mech Rev vol 57, no 4, in: http://appliedmechanicsreviews.asmedigitalcollection.asme.org/.

Grady, D. E. (1995), "Dynamic Properties of Ceramic Materials" Sandia National Laboratories Technical Report, SAND94-3266, February.

Grady, D. E. (1999), "Impact Failure and Fragmentation Properties of Tungsten Carbide", Int. J. Impact Eng. 23, 307-317

Häggblad, Hans-Åke, Hockauf, Matthias, Eriksson, Mikael, Berggren, Carina (2005), "Simulation of high velocity compaction of powder in a rubber mould with characterization of silicone rubber and titanium powder using a modified split Hopkinson set-up", In: Powder Technology. 154(1):33-42.

Lang, Shawn Michael (2012), "Design of a Split Hopkinson Bar Apparatus for use with Fiber Reinforced Composite Materials", All Graduate Theses and Dissertations. Paper 1284, in: http://digitalcommons.usu.edu/etd/1284.

McQueen, R. G., Marsh, S. P., Taylor, J. W., Fritz J. N., Carter, W. J. (1970), "The Equation of State of Solids from Shock Wave Studies, In High Velocity Impact Phenomena", R Kinslow ed., Academic Press.

Pires, A. S. (2012) "Aplicação da compactação por explosivos na produção de compósitos de carboneto de tungsténio". Doctor thesis in Science and Engineering of materials at University of Aveiro.

Proud, W. G., Chapman, D. J., Williamson, D. M., Tsembelis, K., Addiss, J., Bragov, A., Lomunov, A., Cullis, I. G., Church, P. D., Gould, P., Porter, D., Cogar, J. R., Borg, J. (2007), "The dynamic compaction of sand and related porous systems", AIP Conference Proceedings, Vol. 955 Issue 1, pp.1403-1408.

Sharma, S., Chavan, V.M., Agrawal, R.G., Patel, R.J., Kapoor, R., Chakravartty, J.K. (2011), "Split-Hopkinson pressure bar: an experimental technique for high strain rate tests", Head, Scientific Information Resource Division, Bhabha Atomic Research Centre, Mumbai.

Sory, David (2013), "Notch Sensitivity of AISI 4340 in Dynamic Tensile Testing", Mater Thesis, ECAM, Brussels.

Special Metals Corporation (2007), "INCONEL alloy 718", Publication Number SMC-045, in: http://www.specialmetals.com/assets/documents/alloys/inconel/inconel-alloy-718.pdf .

Vogler, T. J., Gluth, J. W., Grady, D. E., (2005), "Dynamic compaction of Tungsten Carbide Powder", Sandia National Laboratories.

Winter, Ron (2009), "Key Concepts of Shock Hydrodynamics", British Crown Owned Copyright.

ANNEX A – EVALUATION OF THE STRESS CONCENTRATION FACTOR

The stress concentration factor, K, can be determined by the following equation for the position of the hoop strain gauge, $(\theta = 0, R = R_e)$, where the hoop stress is required.

$$K = -\left(\frac{\rho^2}{1-\rho^2}\right) + \sum_{n=2}^{\infty}\left[n(n-1)c_n r^{n-2} + (n+2)(n+1)d_n r^n + n(n+1)c_n` r^{-n-2} + (n-2)(n-1)d_n` r^{-n}\right]\cos n\theta \quad (0.1)$$

Where $\rho = R_i/R_e, r = R/R_e$ and the coefficients $c_n, d_n, c_n`, d_n`$ are determined by:

$$c_n = \frac{1}{2(n-1)D}\left[n(\rho^2-1) + (\rho^{2n}-1) - n^2\left(\rho - \frac{1}{\rho}\right)^2\right], \quad (0.2)$$

$$d_n = \frac{1}{2(n+1)D}\left[n^2\left(\rho - \frac{1}{\rho}\right)^2 + n\left(\frac{1}{\rho^2}-1\right) - (\rho^{2n}-1)\right], \quad (0.3)$$

$$c_n` = \frac{1}{2(n+1)D}[n(\rho^2-1) + (\rho^{2n}-1)], \quad (0.4)$$

$$d_n` = \frac{1}{2(n-1)D}\left[n\left(\frac{1}{\rho^2}-1\right) - (\rho^{2n}-1)\right], \quad (0.5)$$

where D is:

$$D = n^2\left(\rho - \frac{1}{\rho}\right)^2 - \left(\rho^n - \frac{1}{\rho^n}\right)^2. \quad (0.6)$$

Only even values of n are used in the preceding equation. The accuracy of the concentration stress factor depends of the number of terms n used where in this case $n = 10$ is enough for this infinite series achieve the stability. The value of K determined for this situation is **6,855**.

ANNEX B – 2D DRAWINGS OF COMPRESSING DYE

2D drawings of compressing dye:

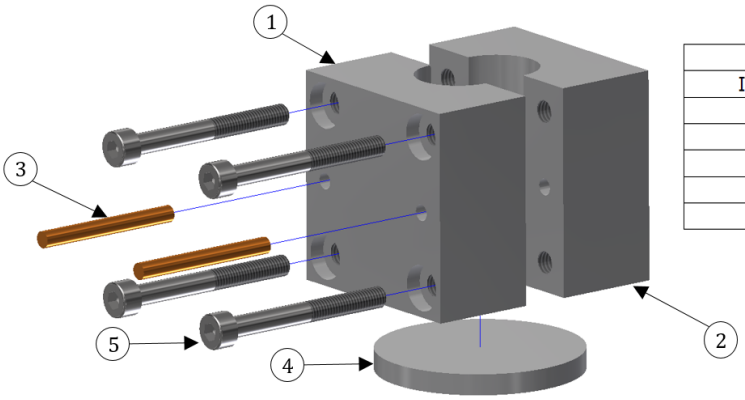

PARTS LIST		
ITEM	QTY	PART NUMBER
1	1	body part 1
2	1	body part 2
3	2	alignment pin
4	1	base plate
5	4	ISO 4762 - M5 x 45

Figure B.1. Explosion view of the compressing dye.

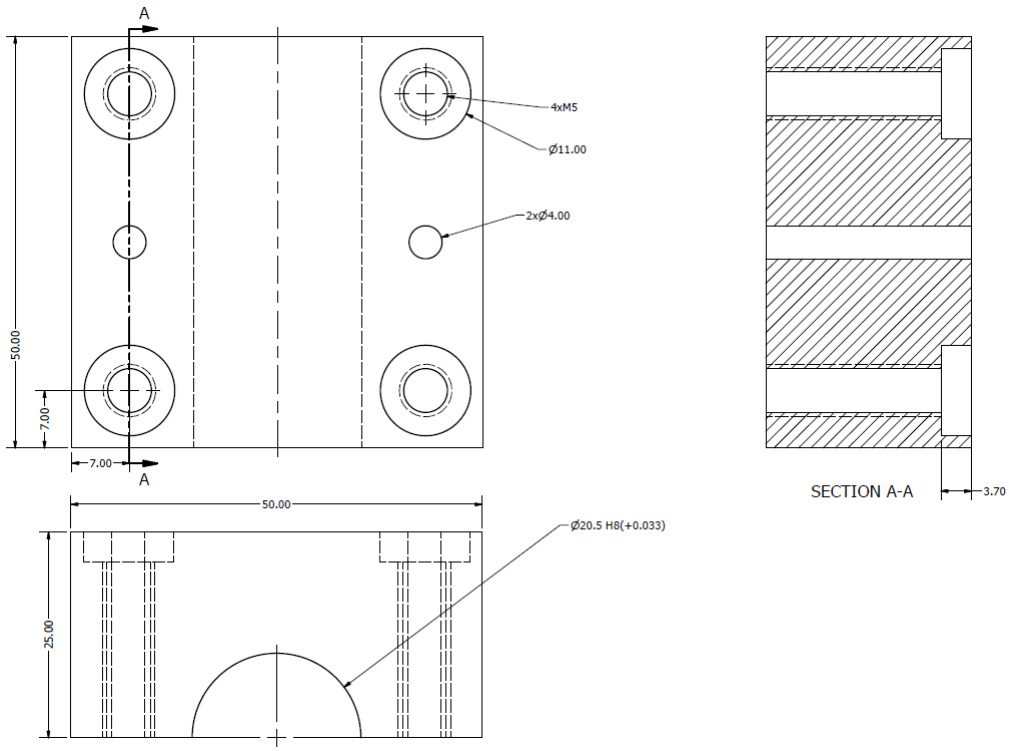

Figure B.2. Body part 1.

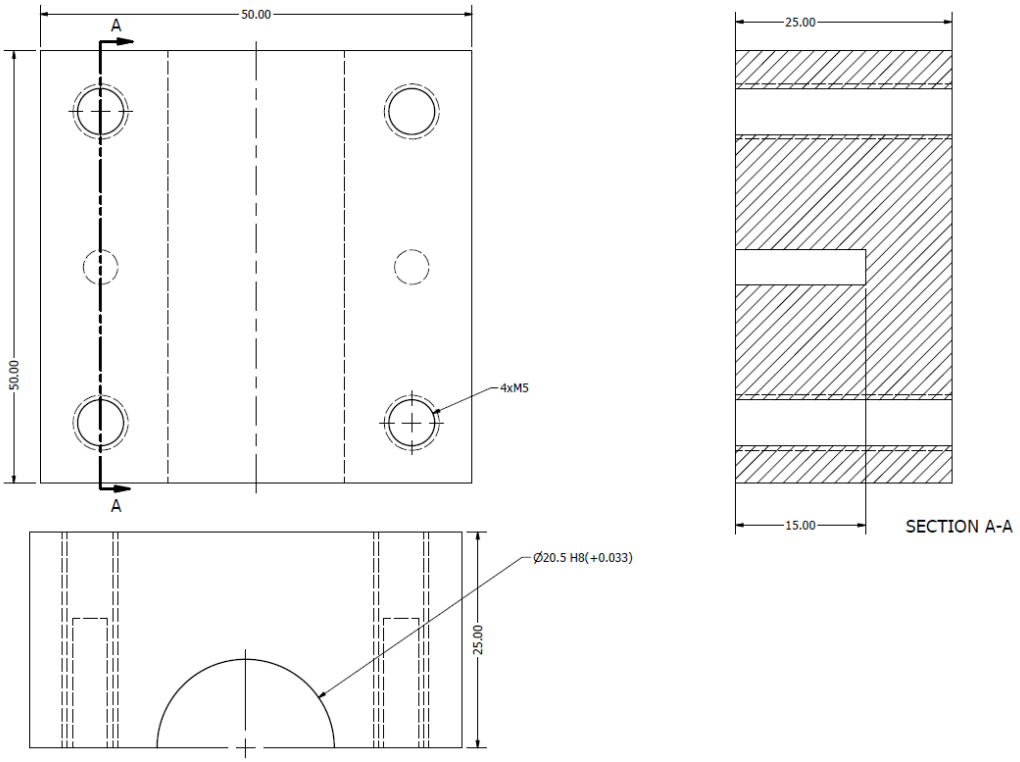

Figure B.3. Body part 2.

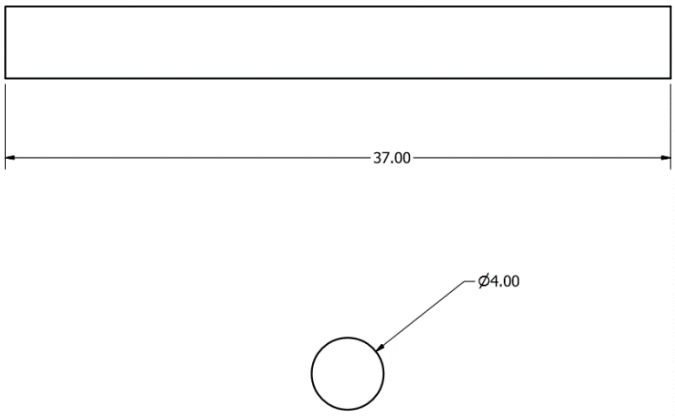

Figure B.4. Alignment pin.

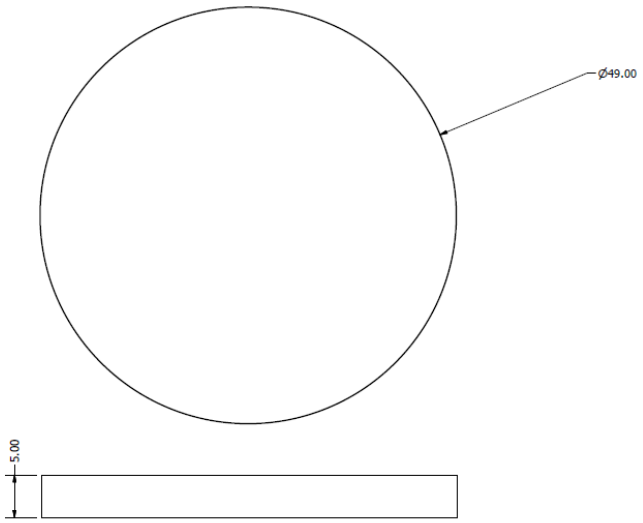

Figure B.5. Base plate.

ANNEX C – 2D DRAWINGS OF THE MULTIPLE TARGET SETUP

2D drawings of the multiple target setup:

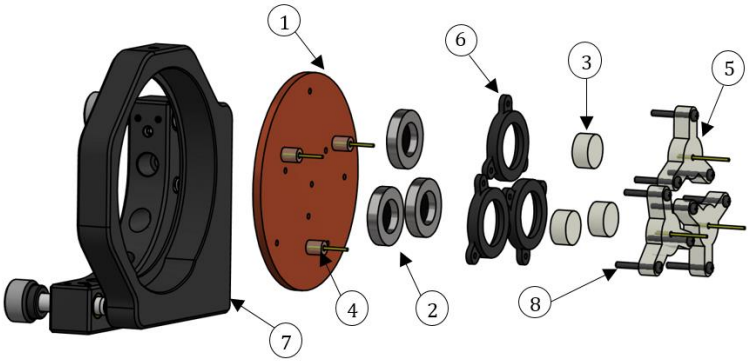

PARTS LIST		
ITEM	QTY	PART NUMBER
1	1	Copper driver
2	3	Ring
3	3	PMMA window
4	3	HetV holder
5	3	PMMA holder
6	3	Ring plastic holder
7	1	Kinemetic mirror mount
8	9	ISO 7045 - M2 x 16

Figure C.1. Explosion view of the multiple target.

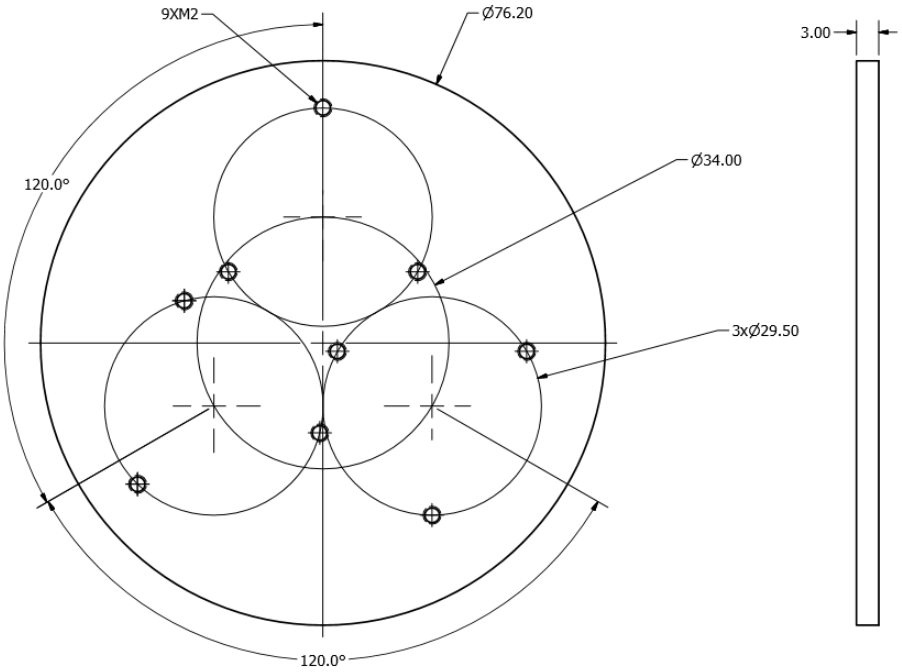

Figure C.2. Copper driver.

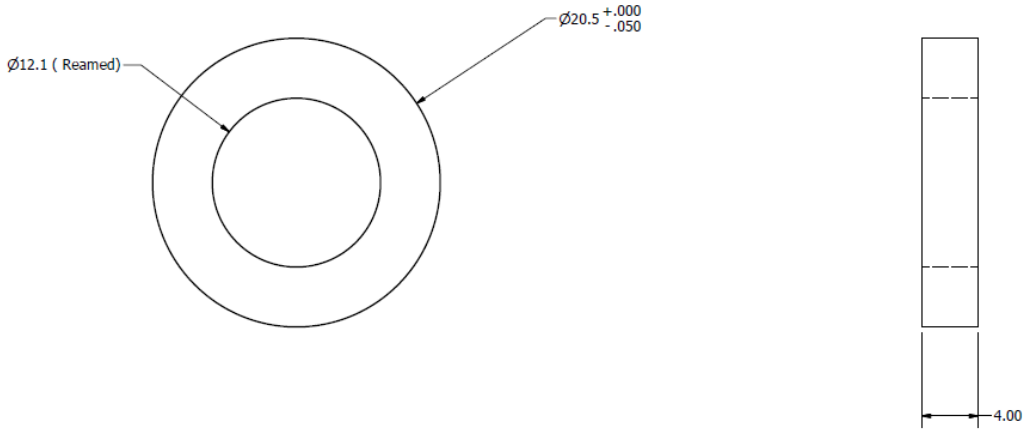

Figure C.3. Ring.

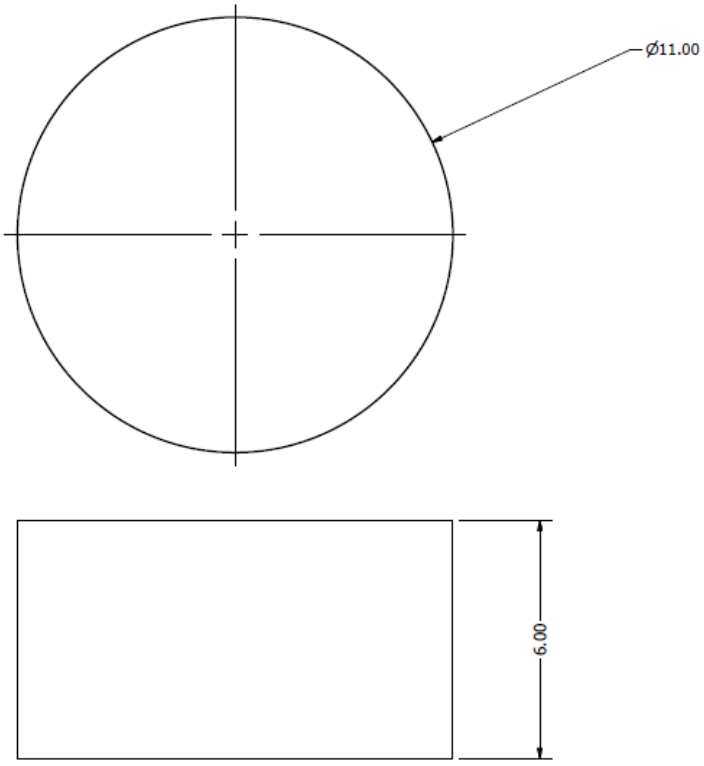

Figure C.4. PMMA window.

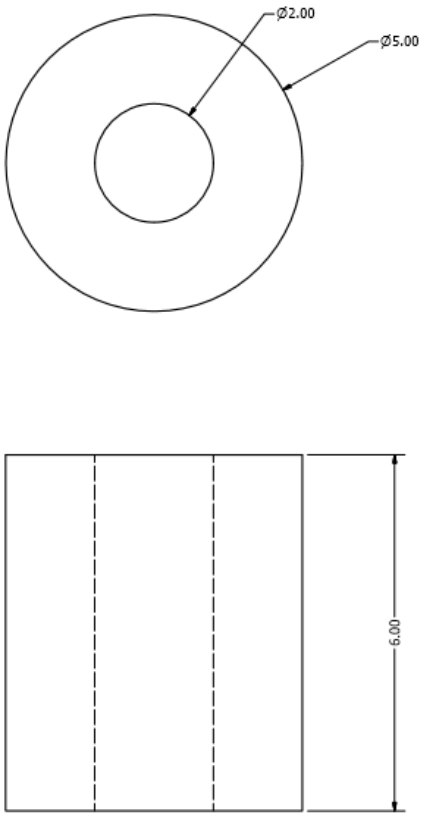

Figure C.5. HetV holder.

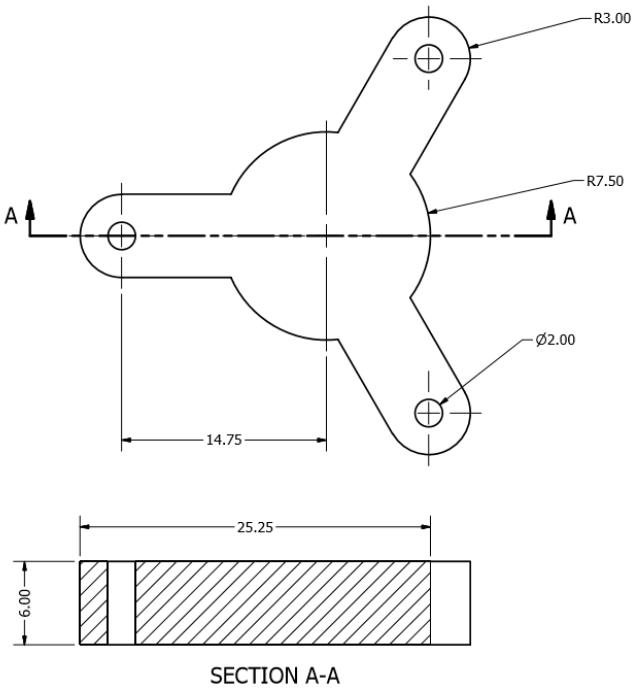

Figure C.6. PMMA holder.

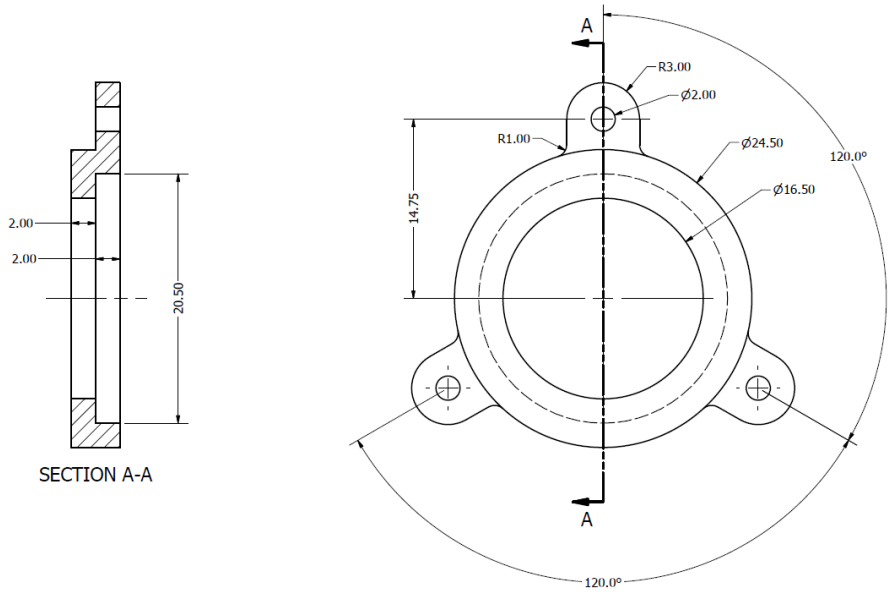

Figure C.7. Ring plastic holder.